Exploring Catalyst Dynamics in a Fixed Bed Reactor by Correlative Operando Spatially-Resolved Structure-Activity Profiling

B. Wollak[a], D. E. Doronkin[b,c], D. Espinoza[a], T. Sheppard[b,c], O. Korup[a,d], M. Schmidt[d], S. Alizadefanaloo[f], F. Rosowski[e], C. Schroer[f,g], J.-D. Grunwaldt[b,c], R. Horn*[a,d]

* Corresponding author

[a] Hamburg University of Technology, Institute of Chemical Reaction Engineering, Eißendorfer Str. 38, 21073 Hamburg, Germany, E-Mail: horn@tuhh.de

[b] Karlsruhe Institute of Technology, Institute for Chemical Technology and Polymer Chemistry, Engesserstr. 18/20, 76131 Karlsruhe, Germany

[c] Karlsruhe Institute of Technology, Institute of Catalysis Research and Technology, Hermann-von-Helmholtz-Platz 1, 76344 Eggenstein-Leopoldshafen, Germany

[d] Reacnostics GmbH, Am Kaiserkai 30, 20457 Hamburg, Germany

[e] UniCat BASF Joint Lab, Hardenbergstraße 36, 10623 Berlin, Germany

[f] Deutsches Elektronen-Synchrotron DESY, Notkestraße 85, 22607 Hamburg, Germany

[g] Department Physik, Universität Hamburg, Luruper Chaussee 149, 22761 Hamburg, Germany

Abstract

Efficient and sustainable optimization of heterogeneous catalytic processes requires a deep understanding of catalyst structure-activity relationships that occur inside catalytic reactors in space and time. Here we introduce a catalytic profile reactor capable of simultaneously measuring spatially-resolved temperature, concentration, and X-ray absorption spectroscopy (XAS) profiles through a catalytic fixed-bed. Using the oxidative dehydrogenation of ethane to ethylene over $MoO_3/\gamma\text{-}Al_2O_3$ as a test reaction, we obtained a detailed picture of local catalyst structure and activity under realistic and well-defined reaction conditions. The concentration and temperature profiles obtained were used to develop a kinetic model. The fit of kinetic models to complete reactor profiles significantly speeds up the development and accuracy of kinetic models required for any reactor design. Further, the kinetic model includes the oxidation state of molybdenum as a descriptor. Hence, we could predict local catalyst oxidation states and validate our model experimentally with spatially-resolved XAS. This provides a quantitative link between catalyst structure and reactivity and allows including catalyst dynamics in reactor simulations. In the current work a widely applicable methodological approach is presented to understand and optimize heterogeneous catalytic processes, e.g. in selective oxidation.

1 Introduction

Light olefins are considered as one of the basic building blocks of the chemical industry [1]. Many different derivatives used in our daily lives are produced from ethylene and propylene. Lower olefins are conventionally produced via steam cracking of a wide range of hydrocarbon (HC) feedstocks [2,3]. Steam cracking is one of the most energy demanding processes in the chemical industry [3]. To meet global demand, ethylene production is expected to increase to more than 200 million tons by 2025 [4]. Changing current processes from endothermic to exothermic pathways reduces the energy required in operation, meeting one of the future challenges of efficient energy consumption. Thus, the selective production of olefins from light alkanes through oxidative dehydrogenation (ODH) in the presence of oxygen and highly selective solid catalysts has evolved to be an attractive alternative to conventional processes [5–8].

A crucial step to substitute existing energy intensive technologies is to optimize performance of heterogeneous catalysts. In addition to design, scale-up and implementation, every industrial catalyst typically undergoes an optimization process of several years. Depending on the process scale, even small increases in yield, selectivity or catalyst stability, or enabling milder operating conditions in terms or pressure or temperature, can have a disproportionately positive effect on energy consumption. The traditional approach to catalyst optimization is by correlating in- and outlet measurements of the reactant and product phase, while often treating the reactor itself as a black box [9]. This unsustainable methodology reflects still the present situation in industrial chemistry and results in a deficiency in fundamental understanding of catalysts. Catalysts are not static materials and show rather dynamic behavior. In simplified terms this means that chemical composition, surface or bulk structure, type and number of active sites and defects, as well as electronic properties of a catalyst change in response to temperature, total pressure or composition of the reaction mixture [10–13]. Catalyst dynamics have a direct impact on catalytic performance, since structural changes on the atomic level also induce changes of the chemical properties, and therefore catalyst performance. Thus, knowledge of catalyst structure-function relationships is required, particularly taking into consideration spatial heterogeneities which often exist within catalysts and reactors at work.

To overcome the lack of such knowledge in ODH processes, many studies focused on the investigation of transition metal oxides in ODH of lower alkanes to olefins [5,8,14]. Transition metal oxide catalysts based on Mo- [15,16] and V [17–19] have shown promising performance in oxidation catalysis, but are rather complex chemical systems. These catalysts participate actively in oxidation reactions and show considerable changes in their redox states. Particular focus is given to the role of different oxide species on catalytic performance, including the lattice, the catalyst surface and the bulk phase oxygen [18, 19]. This could provide essential information to overcome major challenges as for example avoiding the total combustion of lower alkanes to carbon oxides. Basic understanding in selectivity on oxidation was given by Haber's concepts of electrophilic and nucleophilic oxygen [20,21] and Grasselli's ideas on site isolation [22].

In order to incorporate the aforementioned catalyst dynamics in mathematical models and to promote a knowledge-based approach to optimize heterogeneous catalytic reactors, a detailed picture of the catalyst in its actual working state is required. This is a challenging task since reactors are normally opaque and hardly accessible for most catalyst characterization techniques. Thus, the development and application of appropriate *in situ* and *operando* reactors in combination with high spatially and temporally resolved measurements became a focus of attention [9,23,24]. While *in situ* and *operando* methodology has proven highly valuable for addressing catalyst structure in an active state, most studies still neglect heterogeneity or transient behavior in catalytic activity. Since structure and activity are inseparably linked, the lack of spatially-resolved activity measurements still acts as a barrier in catalyst diagnostics and optimization. In recent years, there were many exciting developments in the field of spatially-resolved *operando* spectroscopy of heterogeneous catalysts at synchrotron facilities [25–30].

The development of quartz capillary microreactors with plug flow geometry overcame existing limitations of many spectroscopic cells, which are often kinetically ill-defined [31,32]. One major drawback remains that small sample geometries often restrict product concentration and temperature measurements to the inlet and outlet of the reactor, while local catalyst activity remains unknown. Pioneering work was done by Goguet et al. [33,34] who demonstrated for the first time simultaneous measurement of X-ray absorption spectroscopy (XAS), concentration- and temperature profiles through a powdered catalyst bed under industrial conditions. Here one drawback remains the applied heating system of an unidirectional hot air blower similar to those used in capillary microreactors [35]. By means of hot air, especially in setups using larger sampling geometries, a uniform heating along the catalyst bed and pre-heating gases to higher reaction temperatures are difficult to achieve [36]. Since catalyst structure and local kinetics depend strongly on temperature, uniform and well-defined temperature conditions along the catalyst bed as well as in the gas phase are crucial steps in such operando measurements. Further, quantification of condensable products is often limited due to a missing trace heating. This stimulated the development of a flexible spatial profile reactor for synchrotron measurements using a more sophisticated heating concept. The next level of advanced operando studies is to use the observed data for optimization of catalytic fixed bed reactors by developing macrokinetic models.

This study introduces the design and application of a kinetically well-defined operando spatial profile reactor in lab-scale. The profile reactor is optimized for measuring simultaneously concentration, temperature and XAS through a fixed-bed under industrially relevant conditions. The reaction under investigation is the ODH of ethane to ethylene ($C_2H_6 + ½\ O_2 \rightarrow C_2H_4 + H_2O$ $\Delta H_r°$=-105kJ·mol^{-1}) over MoO_3/γ-Al_2O_3. The chemical system lends itself as a model system and combines the advantages of being relatively well-studied, with relatively low degree of complexity due to only one transition metal of interest. The setup used addresses the challenge to obtain local catalyst activity data, thereby improving the relevance of operando studies. Sample geometries with reaction tubes of up to 4.8 mm inner diameters are used. A uniform heating along the catalyst bed is achieved via direct contact between the reaction tube and a heating block with a sufficient long pre-heating zone for gases. Further, all lines are heated and make quantification with condensable reactants and products feasible.

The aim of this study is to correlate the chemical structure of the catalyst in response to changes in local operation conditions, derived from XAS, with the local chemical potential of the reaction mixture. In addition, a set of catalytic performance studies were performed to obtain a detailed picture of the catalyst under various reaction conditions. Based on the experimental concentration-, temperature- and XAS profiles, a kinetic model of the reaction could be developed which involves the oxidation state of the catalyst as catalyst descriptor. This provides a quantitative link between catalyst structure and reactivity and allows including catalyst dynamics in reactor simulations. The fit of kinetic models to complete reactor profiles significantly speeds up the development and accuracy of kinetic models required for any reactor design. The chosen catalyst system is a useful benchmark to demonstrate the power of this methodology in combined kinetic and spectroscopic studies, particular by means of synchrotron radiation.

2 Experimental

2.1 Catalyst Synthesis

Catalyst samples were prepared by wet impregnation. Two different target weight loadings of 10 and 30 wt% MoO_3 supported on γ-Al_2O_3 were produced. Alumina spheres were provided by Sasol with 1 mm diameter and a specific surface area of 160 m^2/g. Prior to impregnation, γ-Al_2O_3 was crushed and sieved to a particle size of 200-400 µm. Ammonium heptamolybdate tetrahydrate (AHM, $(NH_4)_6Mo_7O_{24}$ x 4 H_2O, 99.0%) from Merck was used as a molybdenum precursor. The required mass of AHM was dissolved in deionized water at a pH of 5.2. This solution was added in 15-20 impregnation steps to the support. In between each impregnation step the solvent was removed in a rotary evaporator (40 °C, 100 mbar, 5 h). After impregnation the catalyst was dried at 120 °C overnight and then calcined at 540 °C for 3 h in synthetic air flow. The calcined catalysts were used for further catalytic tests as-prepared.

2.2 Catalyst Characterization

Standard powder X-ray diffraction (XRD) measurements for qualitative phase composition analysis were conducted using an Empyrean diffractometer from Malvern Panalytical. XRD patterns were recorded over a 2θ range from 10 to 80° using the Kα lines of copper and a PIXcel1D detector. HighScore Plus software and reference patterns from the ICDD database were used for qualitative phase analysis. The specific surface area was determined by N_2-physisorption at 77 K by standard BET analysis with a Quantachrome autosorb iQ instrument.

2.3 Spatial Profile Measurement Technique

The working principle of the spatial profile measurement technique with the profile reactor used in this work is similar to that described in previous publications [24,37]. The main difference is that the catalyst bed is translated vertically, instead of a roto-translational movement of the capillary. The working principle of spatial profiling is illustrated in Figure 1a and shortly summarized as follows: the catalyst bed is packed in a thin-walled reactor tube made of fused silica (OD 6 mm, ID 4-5.6 mm), fixed in position with silica wool plugs. The gases of interest are directed into the reaction tube, regulated by a set of mass flow controllers (MFCs). A preheating zone of 4 cm ensures that the gases are heated to the desired reaction temperature before reaching the beginning of the catalyst bed. A stainless steel or fused silica sampling capillary (OD 700 µm, ID 520 µm), fixed in space, with side-sampling orifices (4 x 50 µm) runs through the center of the tube. A thermocouple is located inside the sampling capillary, with the tip aligned to the orifice (OD 250 µm). Small gas samples are continuously extracted through the orifice and analyzed. Sampling flow rates of approximately 5 % of the total flow rate are taken to ensure negligible disturbances to the hydrodynamic conditions of the reactor. Spectroscopic information is obtained by directing X-rays onto the sample. The probe volume, formed by sampling orifice, thermocouple and X-ray beam remains fixed in space. The reactor tube containing the catalyst bed is shifted laterally along this probe volume with micrometer resolution.

This allows composition and temperature measurement at the very same position at which the catalyst is probed spectroscopically.

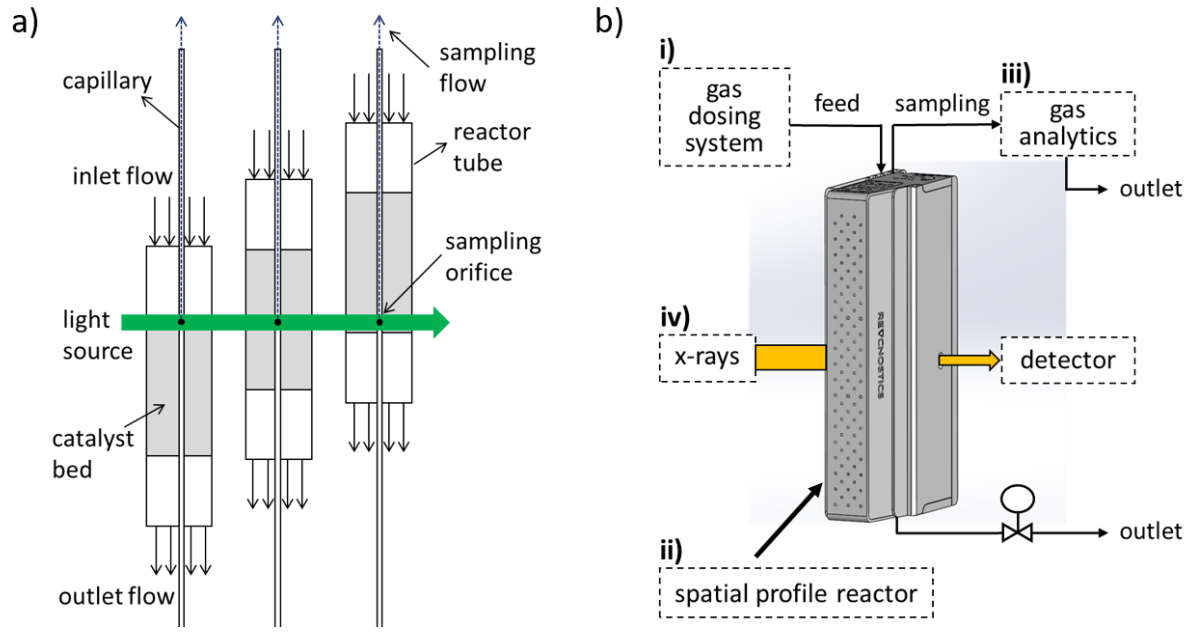

Figure 1: a) Working principle of the spatial profile measurement technique using the spatial profile reactor applied in this work. b) Methodology of simultaneously measured concentration and spectroscopic profiles.

2.4 Spatial Profile Studies

An overview of the experimental setup used to obtain temperature, concentration and spectroscopic gradients inside the fixed bed is given in Figure 1b. The setup consists of four main parts: (i) gas dosing system; (ii) spatial profile reactor; (iii) gas analytics and (iv) a spectrometer (X-ray absorption). The reactants were dosed by a set of MFCs (Bronkhorst GmbH). For catalyst characterization under reaction conditions the **C**ompact **P**rofile **R**eactor (**CPR**, REACNOSTICS GmbH) was used (Figure S1). Gases were analyzed quantitatively by gas chromatography (GC, Agilent 7890B) or mass spectrometry (MS, Hiden HPR 20). Temperature profiles are measured in the center of the catalyst bed with a sheath-thermocouple type K using Inconel as sheath material (TMH GmbH). All transfer lines and the reactor housing were heated up to 200 °C to prevent water condensation in the lines. The developed CPR control system by REACNOSTICS GmbH allows to run the experimental setup (i), (ii) and (iii) fully automatized. XAS was carried out at beamline P64 of the PETRA III synchrotron radiation source at DESY (Hamburg, Germany). Further details about the experiments performed in this work are described in the respective experimental subsections.

2.4.1 Catalyst Activity

Catalyst activity profiling were performed in this work using the fully automatized experimental setup consisting of three MFCs (i), CPR (ii) and a MS for quantitative gas analysis (iii) as described in the previous Section 2.4. The MS was equipped with a heated capillary inlet to prevent water condensation. A Faraday detector operating in Multiple Ion Detection (MID) mode was monitoring the following mass to charge ratios (m/z): C_2H_4 (27), CO (28), C_2H_6 (30), O_2 (32), Ar (40) and CO_2 (44). Signal contributions from other reaction components to peaks

27 and 28 were corrected by subtracting the contributions of HCs and CO_2 to these signals. Further details in quantification are shown in supplementary information. By using the described methodology carbon and oxygen balances for all profile runs were closed with average deviations of up to 5 %.

All catalytic tests were performed using a 30 wt% MoO_3 supported on γ-Al_2O_3 catalyst. The reaction tube had an inner diameter of 4 mm. Reactor pressure was 1 bar. Reaction temperatures were measured in the reactor heating block and in the center of the catalyst bed. Measured temperatures in the catalyst bed are 10-15 K below the set temperatures depending on the level of conversion. Temperatures in the heating block were used as reference points in all measurement plans. Before starting each individual profile run, the catalyst was pretreated to a reference state for 1 hour in a mixture of O_2:inert = 20:80 at 480 °C. After that, the reactant feed mixture was adjusted according to the experimental kinetic plan, and a time of 90 minutes was given to reach steady state.

Catalyst activity profiling measurements can be divided into two parts. The **first part** investigates the influence of the main reaction parameters e.g. effect of feed concentrations (C_2H_6, O_2) and reaction temperature on catalytic performance. Key objectives were to test for catalyst stability, reproducibility of the sampling technique through the catalyst bed and to define scan ranges of the aforementioned parameters. Based on the previous tests, **the second part** includes two face centered central composite design plans with each two factors. Both plans include the variation of O_2 feed concentration as factor. The second factor is to test for variations in either C_2H_6 or C_2H_4 as feed component. Reactor temperatures were varied in five steps from 480 to 530 °C for each HC but not included as parameter in the measurement plan. Goal is to develop a kinetic model capable of representing the oxidation zone (gaseous O_2 present), which is relevant in industrial applications. Therefore, feed concentration variations are required to determine reaction orders as well as the variation in temperature to calculate activation energies. The kinetic model development is presented in Section 2.4.2.

1st part: Catalytic tests were conducted using a catalyst bed length of 30 mm and a catalyst sieve fraction of 200-400 µm. A total flow rate of 30 ml/min that corresponds to a maximum GHSV of 4714 h^{-1} at the reactor outlet was applied. An overview of the experimental plan is shown in Figure 2. Ten profile runs were performed, including eight individual runs (P1-8) and two replicates (R1 + R8). Inlet concentrations of O_2 (factor 1) and C_2H_6 (factor 2) ranged from 7.5 to 12.5 % or 75 to 125 mbar, respectively. The temperature as the third factor was varied from 480 to 530 °C in two levels.

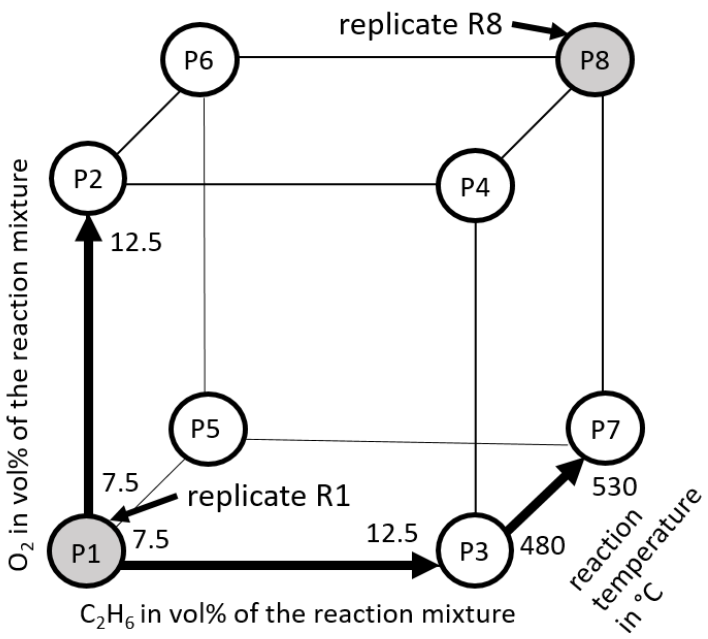

Run	vol% of C_2H_6	vol% of O_2	T in °C
P1	7.5	7.5	480
P2	7.5	12.5	480
P3	12.5	7.5	480
P4	12.5	12.5	480
P5	7.5	7.5	530
P6	7.5	12.5	530
P7	12.5	7.5	530
P8	12.5	12.5	530
R1	7,5	7,5	480
R8	12,5	12,5	530

Figure 2: Schematic representation of the two-level, three-factor experimental design plan with $2^3 = 8$ spatial profile measurements. Factor 1: Vol% of O_2 in the reaction mixture from 7.5-12.5 %; Factor 2: Vol% of C_2H_6 in the reaction mixture from 7.5-12.5 %; Factor 3: Reactor target temperature from 480-530 °C. Reaction conditions: 1 bar, catalyst bed length 30 mm, 30 ml/min.

2nd part: A catalyst bed length of 32 mm was applied (maximum GHSV C_2H_6: 4399 h^{-1}; C_2H_4: 5944 h^{-1}). Due to a high C_2H_4 reactivity, the flow rate was increased from 30 to 40 ml/min in the C_2H_4 measurement plan. Concentration profiles were measured on 19 positions along the catalytic bed, with steps of 3 mm between sampling points. A higher point density of 1 mm was used in the first 6 mm of the catalytic bed in order to properly measure the initial rate of consumption/production of relevant compounds.

An overview of all experiments performed in the second part is given in Figure 3. The left picture shows 13 profile runs (P5-13) that were performed to study the effect of O_2 and C_2H_6. The four profile runs at the cube corners (P5-8) were measured in the 1st part. To obtain the face centered central composite design, all axial measurement points projected on the surfaces (P9-P12) and the central point (P13) were measured in addition. Further, four replicates of the central point (R13a-d) were made. Replicates were uniformly distributed through the campaign to test for stable operation. The effect of C_2H_4 was studied within 13 profiles (P14-22) and again four replicates of the central point (R18a-d). In the end of each measurement plan four more runs were subsequently conducted at the central point at different temperatures 480, 500, 520 and 540 °C (T13a-d and T18a-d), respectively.

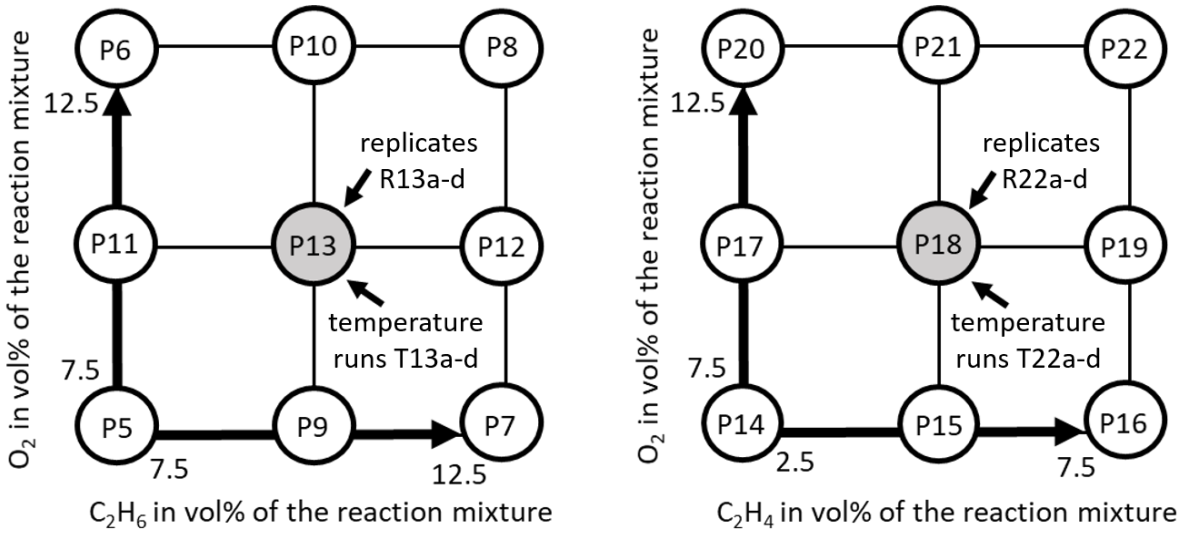

Figure 3: Schematic representation two three-level, two-factor experimental design plans with $3^2 = 9$ spatial profile measurements. Factor 1: Vol% of O_2 in the reaction mixture at 7.5, 10, 12.5 %; Factor 2: Vol% of C_2H_x in the reaction mixture from 7.5, 10, 12.5 % (left) and 2.5, 5, 7.5 % (right). Reaction conditions: 530 °C, 1 bar, catalyst bed length 32 mm, C_2H_6: 30 ml/min; C_2H_4: 40 ml/min.

The presence of external and internal transport limitations were excluded by calculating the dimensionless Mears and Weisz-Prater criteria. Radial temperature gradients of the reactor itself are negligible and evaluated by following the criterion of Mears [38]. Further information is given in the supplementary material.

2.4.2 Kinetic Modeling

Reactor Model

A 1D pseudo-homogeneous Plug Flow reactor with constant density, constant temperature and constant pressure was modeled in order to perform parameter estimation:

$$\frac{dC_i}{dz} = \frac{(R_{i,net} * \rho_{bed})}{U_z} \quad (1)$$

Where C_i is the molar concentration of component i, $R_{i,net}$ is the weight base net rate of consumption / production of component i, ρ_{bed} is the bed bulk density, z is the axial position along the catalytic bed and U_z is the gas velocity in axial direction. Finally, the net rate of species i is determined:

$$R_{i,net} = \sum_j \nu_{ij} * r_j \quad (2)$$

Where ν_{ij} is the stoichiometric coefficient of species i in reaction j, and r_j is their respective rate.

Profile Data Fitting

The general fitting problem consists of solving a set of ordinary differential equations (ODEs) derived out of Eq.(1) for all components involved in the reaction system. Thus, in this work a Matlab script (Matlab®, v2019a) was developed to perform an integral data analysis of the concentration profile measurements presented in Section 2.4.1. The Matlab script solves a set

of ODEs with molar concentrations as response variables by an already implemented solver ode23s. Once the ODEs are solved, the optimization algorithm lsqcurvefit was used to evaluate the difference between the experimental data and the currently predicted data. The optimization algorithm includes a nonlinear fitting procedure according to Eq.(3) that calculates the difference between predicted molar concentration $F(p, pdata_i)$ and its experimental values $cdata$ from the profile measurements. The goal is to find the kinetic parameter p that minimizes Eq. (3).

$$\min_p \|F(p, pdata) - cdata\|_2^2 = \min_p \sum_p (F(p, pdata_i) - cdata_i)^2 \quad (3)$$

Additionally, a constrained nonlinear optimization algorithm was applied in the program in order to ensure that estimated kinetic parameters are non-negative numbers. As soon as the algorithm finds a reasonable solution, the optimization stops and the final values of kinetic parameters (fitting parameters) as reaction order, pre-exponential factor and activation energies are obtained.

Initial guesses of pre-exponential factors and activation energies were important in the fitting procedure because they allow to find the global minimum of the system instead of local minimum points. Activation energy guesses are obtained from Arrhenius plots by using concentration profiles obtained from the temperature runs P14-17 (C_2H_6) and P27-30 (C_2H_4) in the range of 480-540 °C. The experimental concentration profiles were fitted simultaneously as complete reactor profiles in the developed script. In simple terms, each species concentration profile includes eleven data points measured through the catalyst bed (eleven distinguished conversion levels). The optimization algorithm minimizes in an iterative process (predicted vs. experimental) the sum of squares of all data points within one species concentration profile for five different species (C_2H_6, C_2H_4, CO, CO_2 and O_2) at four temperatures together (in total 20 profiles). Hence, the profile data at 480-540 °C are not evaluated successively which as a result provide only one set of fitting parameters. In the present work the set temperature was used for fitting the profiles but in principle it is possible to incorporate the temperature profile in the fitting. This will be subject of further work.

In order to avoid parameter correlation between the pre-exponential factor and activation energy of the Arrhenius equation, a reparametrized form of this equation was employed.

$$k = k_{ref} \exp\left[-\frac{E}{R}\left(\frac{1}{T} - \frac{1}{T_{ref}}\right)\right] \quad (4)$$

Where k_{ref} represents the specific reaction rate at the reference temperature T_{ref} which for this study is represented as the average temperature in the range of 480-540 °C.

$$k_{ref} = A_o \exp\left[-\frac{E}{R\,T_{ref}}\right] \quad (5)$$

Mars-van Krevelen Model

In order to obtain a deeper physical insight into our reaction system, a Mars-van Krevelen (MVK) approach was followed [39]. The kinetic model developed in this work considers a set of reactions presented in Table 1. The main reaction is the ODH of ethane to ethylene

(Reaction step 1). Additionally, the network includes the partial and total combustion of ethane and ethylene to CO_x as shown in Reactions 2-5. Finally, the reoxidation of the catalyst by gas phase oxygen is taken into account and represented by Reaction step 6. Here, the reaction constant is represented by k_i, the molar fraction of component i in the gas phase by y_i and the fraction of oxidized catalyst sites by θ_{ox}. From a chemical point of view, the latter is defined in the way that $\theta_{ox} = 1$ represents the catalyst in its fully oxidized state und thus MoO_3. Inversely, if $\theta_{ox} = 0$ the catalyst is reduced, corresponding to MoO_2. Further, each reaction has two fitting parameters (A_0 and E_a). In addition, Reaction 6 contains the reaction order n as fitting parameter, describing how sensitively the reoxidation depends on the partial pressure of oxygen.

Table 1: Considered reaction steps in the MVK model for ODH of ethane.

	Reaction step	Rate expression
1	$C_2H_6 + O_l \xrightarrow{k1} C_2H_4 + H_2O + l$	$r_1 = k_1 y_{C_2H_6} \theta_{ox}$
2	$C_2H_6 + 5O_l \xrightarrow{k2} 2CO + 3H_2O + 5l$	$r_2 = k_2 y_{C_2H_6} \theta_{ox}$
3	$C_2H_6 + 7O_l \xrightarrow{k3} 2CO_2 + 3H_2O + 7l$	$r_3 = k_3 y_{C_2H_6} \theta_{ox}$
4	$C_2H_4 + 4O_l \xrightarrow{k4} 2CO + 2H_2O + 4l$	$r_4 = k_4 y_{C_2H_4} \theta_{ox}$
5	$C_2H_4 + 6O_l \xrightarrow{k5} 2CO_2 + 2H_2O + 6l$	$r_5 = k_5 y_{C_2H_4} \theta_{ox}$
6	$l + 0.5O_{2(g)} \xrightarrow{kox} O_l$	$r_{ox} = k_{ox} {y_{O_2}}^n \theta_{red}$

To derive the modeling equations for each one of the fitted components in Eq.(1), the following assumptions were made in the MVK approach:

1. Only one active lattice oxygen species exists.

$$1 = \theta_{ox} + \theta_{red} \tag{6}$$

2. The catalyst is in steady state, meaning that the rate of catalyst oxidation equals the rate of catalyst reduction. This can expressed by the following equation:

$$R_{ox} = R_{Red} \tag{7}$$

By considering the aforementioned assumptions and the site balance equation, the following equation for the determination of the oxidized sites coverage was derived.

$$\theta_{ox} = \frac{k_{ox} {y_{O_2}}^n}{k_{ox} {y_{O_2}}^n + (k_1 + 5k_2 + 7k_3) y_{C_2H_6} + (4k_4 + 6k_5) y_{C_2H_4}} \tag{8}$$

2.4.3 Operando X-ray Absorption Spectroscopy

During the operando XAS experiment the 10 wt% MoO_3 supported catalyst was used. The reaction tube had an inner diameter of 4.8 mm. The reactant feed consisted of ethane, oxygen and as diluent a mixture of He in Ar with gas compositions of C_2H_6:O_2:inert = 10:10:80. The reaction conditions were set to 530 °C at ambient pressure and a total flow rate of 20 ml/min corresponding to a GHSV of 1646 h^{-1}. Gas compositions of He, C_2H_6, C_2H_4, O_2, CO and CO_2 were analyzed with a GC with four gas channels installed. A MolSieve column was used to separate the permanent gases He, H_2, CO and a Plot Q column to separate C_2H_6, C_2H_4 and CO_2, connected to a thermal conductivity detector (TCD). Water and CO were calculated with the atom species balance of the reaction mixture. Helium was used as internal standard.

XAS experiments were carried out at beamline P64 at the PETRA III synchrotron radiation source (DESY, Hamburg, Germany) [40]. A picture of the experiment is shown in supplementary materials (Figure S2). A modified CPR optimized for synchrotron X-rays at beamlines was used allowing measurements in transmission mode for XAS. The modification consists of a slotted heating block for the X-ray beam to penetrate through the catalyst bed. Precise alignment of the X-ray beam, the thermocouple and the orifice in the sampling capillary was ensured by laser alignment in combination with micrometer precision stages. The position of the measurement volume in the catalyst bed was carefully determined moving the reactor relative to the X-ray beam in horizontal and vertical direction.
XAS experiments in terms of X-ray absorption near edge structure (XANES) and extended X-ray absorption fine structure (EXAFS) were carried out in transmission mode around the Mo K-edge (20 keV). Energy of the incident X-rays was selected by a Si(111) double crystal monochromator and higher harmonics were rejected by a pair of Rh-coated mirrors. Scans were performed in continuous mode (1300 eV in 300 s). The beam size was approx. 0.5 mm^2. The incident and transmitted beam intensity were monitored using a series of three ionization chambers. Spectra of a Mo foil placed between the second and third ionization chamber (reference channel) were measured simultaneously with operando data for energy calibration.

Athena software was used for calibrating and normalizing all spectra, and for subtracting EXAFS background [41]. The k^1-, k^2-, and k^3-weighted EXAFS functions were Fourier transformed (FT) in the k range of 2.5-15.0 $Å^{-1}$ and multiplied by a Hanning window with sill size of 1 $Å^{-1}$. The FT EXAFS spectra are shown without phase shift correction. The structural models were based on MoO_2 and MoO_3 oxide structures (ICSD collection codes 23722 and 80577). The structure refinement was performed using the Artemis software (IFFEFIT) [41]. Firstly, the corresponding theoretical backscattering amplitudes and phases were calculated by FEFF 6.0 [42]. The theoretical data were then adjusted to the experimental spectra by the least square method in R-space between 1.0 and 3.2 / 4.5 Å (beginning / end of the catalyst bed). The amplitude reduction factor (S_0^2 = 0.95) was estimated by fitting the Mo foil reference spectrum to the corresponding structural model (ICSD collection code 52267) and then the coordination numbers, interatomic distances, energy shift (δE_0) and mean square deviation of interatomic distances (σ^2) were refined. The absolute misfit between theory and experiment was expressed by ρ.

Linear combination analysis of the XANES profile was performed in the range of 19980 to 20030 eV using internal references (spectra measured at positions at 2 and 34 mm corresponding to the beginning and end of the catalyst bed). Error bars from the fits with internal references were within ±0.4%.

3 Results and Discussion

3.1 Catalyst Characterization

The resulting diffraction patterns of the ex-situ analysis of the 10 and 30 wt% calcined catalyst confirm orthorhombic crystal structure of MoO_3 for both weight loadings (ICCD: 98-015-8256) [15]. Diffraction patterns are shown in supplementary materials (Figure S3). BET analysis showed that coating reduced the specific surface area of the 10 wt% MoO_3 catalyst to 147.66 m^2/g and of the 30 wt% to 137.91 m^2/g, compared to the initial value of 160 m^2/g for the pure support. The observation is in accordance to literature and could be attributed to the blocking of narrower alumina support pores, which is more strongly apparent with higher weight loadings [15,43]. Corresponding adsorption/desorption curves are shown in the supplementary information (Figure S4).

Pictures of the freshly synthesized material during calcination at 540 °C in synthetic air flow (a), at room temperature after calcination (b) and the color gradient upon reaction (c) are displayed in Figure 4 (representing the 30 wt% catalyst). The catalyst shows the characteristic yellow color of monoclinic β-MoO_3 during calcination (a) [44,45]. Afterwards, during cooling down the catalyst turns white, indicating a phase transformation of monoclinic to orthorhombic α-MoO_3 (b) [44,45]. Upon reaction a color gradient from gray to black along the axial position of the catalyst bed and in the flow direction is observed (c). The clear manifestation of the color gradient is further discussed in Section 3.3.2.

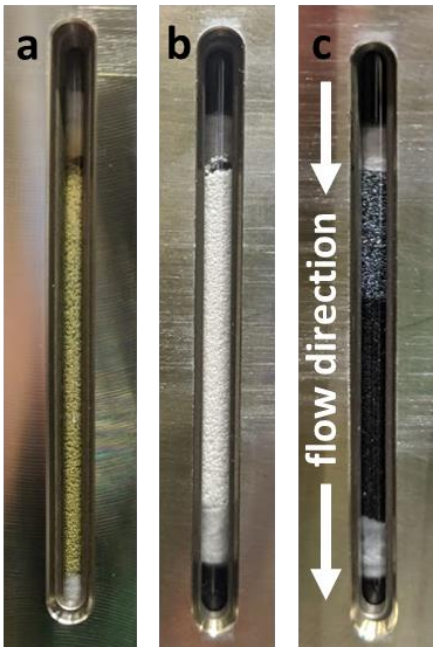

Figure 4: The pictures show the 30 wt% MoO_3 supported catalyst on γ-Al_2O_3 and the clear manifestation in color at different conditions. a) During calcination at 540 °C and synthetic air flow. b) At room temperature after calcination. c) Color gradient upon reaction in flow direction.

3.2 Catalyst Activity Profiling

3.2.1 Stability and Reproducibility Tests

The first experimental part comprises eight profiles and two replicates (Section 2.4.1). In between the original profile (P8) and its replicate (R8) was 40 hours measurement time. Results obtained from the profile (P8) and its replicate (R8) at 530 °C are displayed for all components in Figure 5. By using spatially resolved concentration measurements, local gas compositions through the catalyst bed could be obtained. To illustrate this point, the traditional black box approach of reactor in- and outlet measurements can only provide global information outside the lower (0 mm) and upper (30 mm) range of the black lines, which make accurate correlation between catalyst-structure function relationships more difficult. The reaction mixture is composed of the feed components C_2H_6 and O_2 (a), the main products ethylene and water (b), as well as the undesired carbon oxides CO (c) and CO_2 (d). A good match is shown between replicates and original data throughout all species. Minor deviations are observable in CO that contains mass contributions from C_2H_6, C_2H_4 and CO_2 in quantification with MS. H_2O was the only species calculated from mass balance. The replicate experiments allow to deduce stable catalyst performance through various reaction conditions in the measurement campaign (gas compositions, temperatures). Additionally, they demonstrate stable and reproducible operation of the spatial profile reactor (precise positioning, heating) and of the profile measurement technique. Thus, strong impacts on the catalyst bed by repetitive moving of the sampling capillary through the catalyst bed can be excluded. For example the latter could have led to changes in the catalyst particle size by crushing catalyst particles. As a result smaller particles could block the sampling orifice resulting in variations of sampled gas amounts which in turn disturb hydrodynamic conditions of the reactor. Further, smaller particles compact the bed leading to different catalyst mass per sample position. The aforementioned effects have strong impacts on profile shape and would be clearly observable if they had occurred.

MS analytical deviations at low conversion levels (< 5%) disturb the shape of the selectivity profiles in the very beginning of the catalyst (Figure 5 f). For example the ethylene profile shows a maximum at position 6 mm, which is an analytical artifact. At early bed positions, the molecular flow of reactants tends to zero, therefore minor deviations of these values lead to a large impact on selectivity, obtained via Equation S5. In the same way, selectivity profiles of CO and CO_2 are affected.

The parameter field of C_2H_6 and O_2 inlet concentrations with 7.5 and 12.5 %, respectively, were in a good range to separate conversion profiles clearly from each other. Temperature studies revealed that further tests should not be performed below 480 °C since conversion levels of C_2H_6 and O_2 less than 10 % were obtained. The results of P1 and its replicate R1 at 480 °C are shown in supplementary information (Figure S5). In addition, precise calibration of the reaction system is observable by almost equimolar inlet compositions.

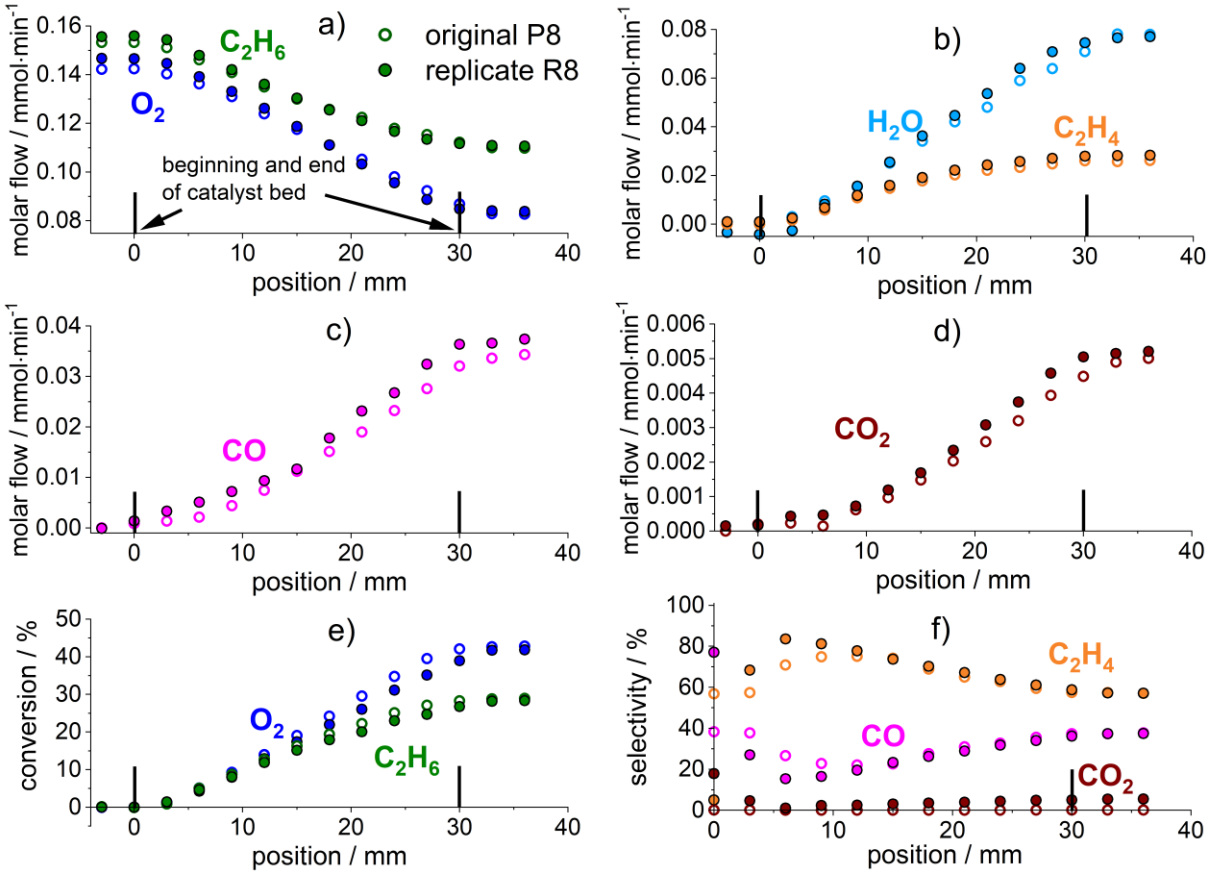

Figure 5: Profile runs measured in the 1st measurement design plan are shown of the original profile (P8) and its replicate (R8) measured at the central point. a-d) Profiles of all species in molar flow rates; e) Conversion profiles of C_2H_6 and O_2; e) Selectivity profiles of C_2H_4 and CO_x. Reaction conditions: C_2H_6/O_2:12.5:12.5, 530 °C, 1 bar, 30 mm catalyst bed, 30 ml/min, 30 wt% MoO_3/γ-Al_2O_3.

The temperature profile results obtained at the central points in the C_2H_6 and C_2H_4 kinetic plan are shown in the supplementary information (Figure S6). Temperature replicates show a good match with minor deviations in the range of 1 °C indicated by error bars. The experimental set temperature assigned to both experiments was 530 °C. The measured temperature in the capillary in the center of the catalyst bed is about 10 °C lower (pos 0 mm) than the set temperature. Depending on the degree of conversion and involved reactions, the temperature raises slightly within the catalyst bed. Temperature raises are below 5 °C feeding C_2H_6 or below 10 °C feeding C_2H_4 and hence, fair isothermality is observed. Temperature profiles obtained at different temperature levels are presented in Section 3.2.3.

3.2.2 Variation in Feed Concentrations

In order to test for feed effects and activation energies required in the kinetic model, factors were varied in the second experimental part on three concentration and five temperature levels. Furthermore, it was observed that experiments feeding C_2H_4 were needed to evaluate the contributions of this species towards CO_x production. Thus, two face centered central composite design plans, one for each HC, were performed. One measurement plan consists of thirteen profiles, including four replicates of the central point and additionally four profile runs at 480, 500, 520 and 540 °C at the end of the measurement campaign. Further details are stated in Section 2.4.1. The four replicates were evenly distributed throughout the measurement plan

to ensure system stability over the whole measurement campaign of 10 days of operation. The original profiles and replicates for all species across both measurement plans exhibit only minor deviations, as demonstrated in the previous Section 3.2.1. The data are shown in Figure S7 and Figure S8.

Figure 6 shows an overview of the profile runs in the second measurement plan performed with variation in O_2 (1st row) and C_2H_6 (2nd row) from 7.5 to 12.5 % for each species. Apparently, no effect of O_2 feed variations on C_2H_6 consumption (a) or C_2H_4 production (c) are observable. These observations indicate that C_2H_6 consumption rate has a low reaction order with respect to O_2 concentration. Thus, processes related to oxygen can be considered as fast.

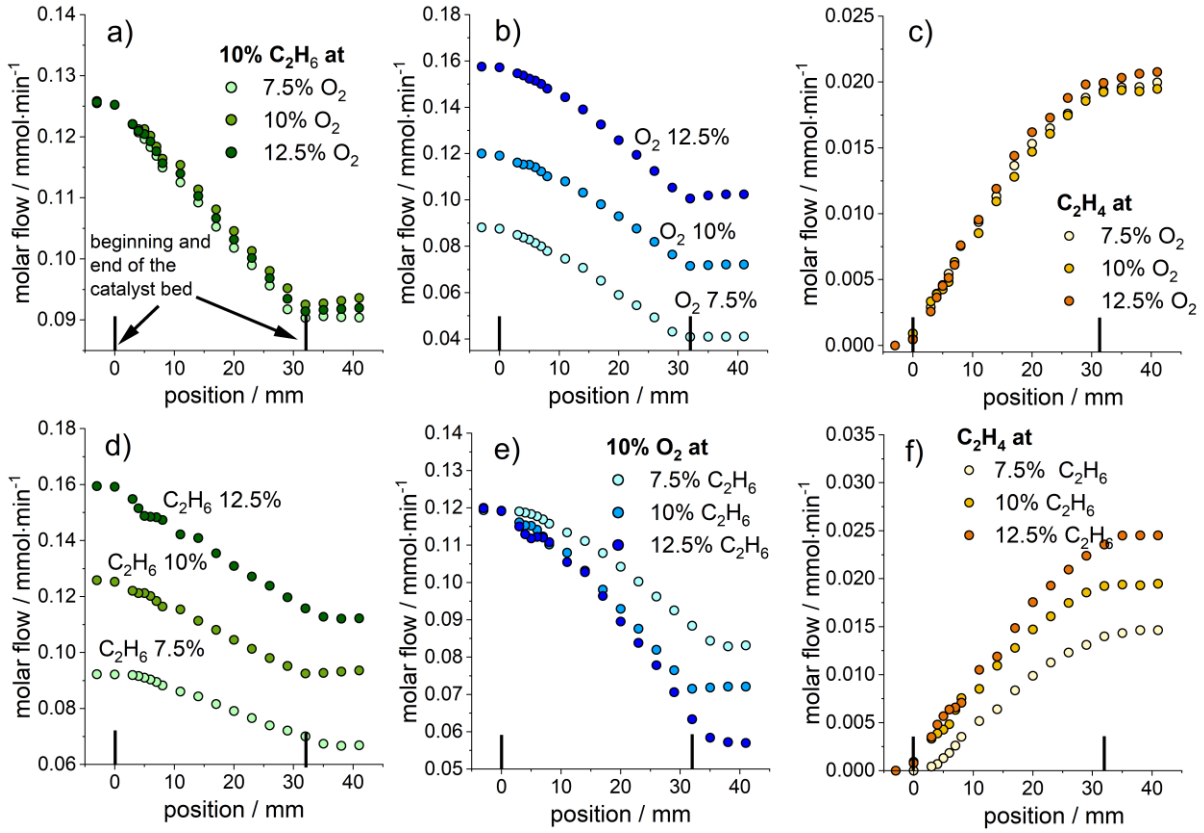

Figure 6: Feed variations of O_2 (1st row) and C_2H_6 (2nd row) at reactant concentrations of 7.5, 10 and 12.5 % (P9-13). All percentage values are in a molar base. (a,d) C_2H_6; (b,e) O_2; (c,f) C_2H_4 concentration profiles. Reaction conditions: 530°C, 1 bar, 32 mm catalyst bed, 30 ml/min, 30 wt% MoO_3/γ-Al_2O_3.

When looking at species concentration profiles performed with different C_2H_6 feed compositions (Figure 6, 2nd row), a clear impact on O_2 and C_2H_4 are observed. An increasing C_2H_6 concentration enhances O_2 consumption (e) and olefin formation (f) along the catalytic bed. The increase in O_2 consumption slows down with increasing C_2H_6 concentration as seen by comparing the 7.5, 10 and 12.5 % C_2H_6 profiles in Figure 6 e).

Figure 7 shows an overview of C_2H_6 (a, d) and O_2 (b, e) conversion profiles as well as C_2H_4, CO, CO_2 selectivity profile runs with variation in O_2 (1st row) and C_2H_6 (2nd row) from 7.5 to 12.5 % for each species. As expected, product selectivity of C_2H_4 within one profile decreases with an increase in ethane consumption (along the catalyst bed), while selectivity towards the

undesired carbon oxides CO and CO_2 increases. In response to the applied feed variations, no clear change on selectivity in between the different profile runs is observable.

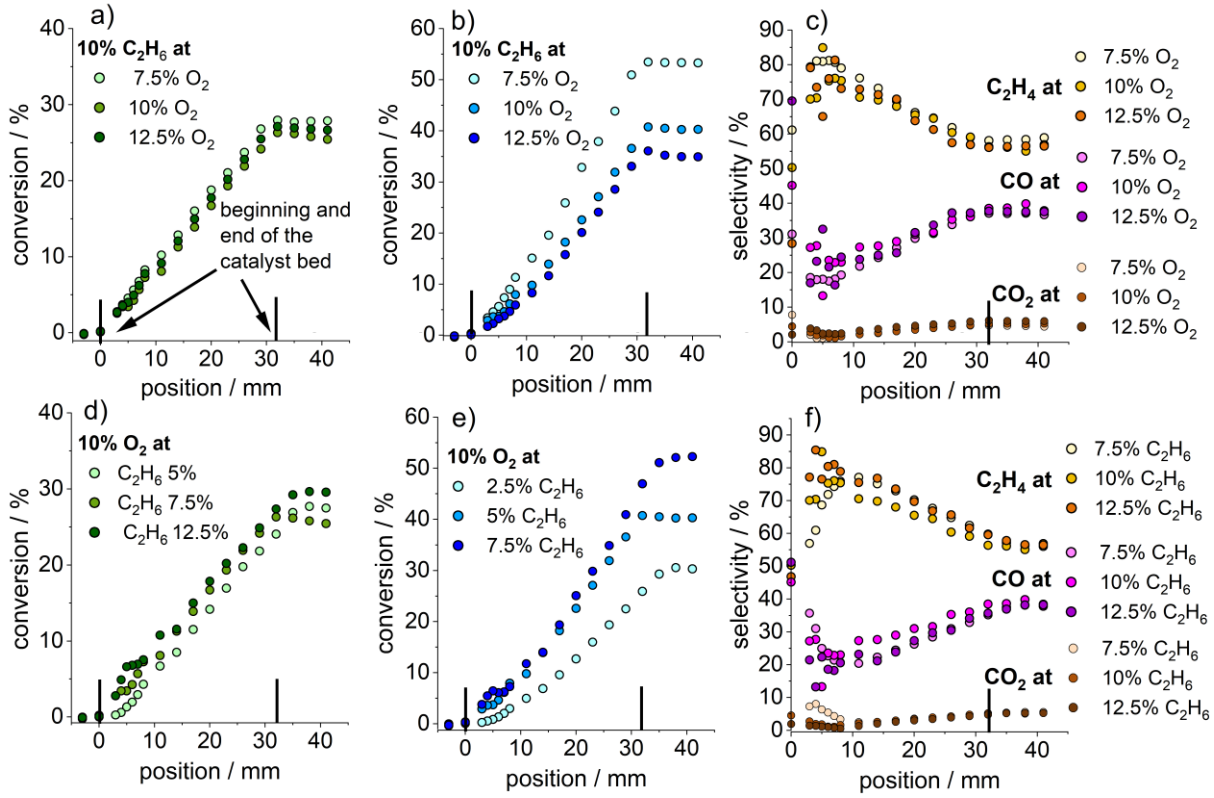

Figure 7: Feed variations of O_2 (1st row) and C_2H_6 (2nd row) at reactant concentrations of 7.5, 10 and 12.5 % (P9-P13). All percentage values are in a molar base. (a,d) C_2H_6; (b,e) O_2 conversion profiles. (c,f) C_2H_4, CO, CO_2 selectivity profiles. Reaction conditions: 530°C, 1 bar, 32 mm catalyst bed, 30 ml/min, 30 wt% MoO_3/γ-Al_2O_3.

Similar observations are made varying C_2H_4 and O_2 feed compositions. Changes in oxygen feed composition from 7.5 up to 12.5 % showed no effect over ethylene and CO_X concentration profiles stating that C_2H_4 consumption rate is of low reaction order with respect to O_2 concentration. This result points out to the fact that C_2H_4 side reactions involve a similar mechanism as in the case of ODH of ethane. Whereas an increase in feed C_2H_4 from 2.5 to 7.5 % leads to an increase on its rate of consumption from 34.5 to 45.3 % and oxygen conversion levels from 19.8 to 73.1 %. Ethylene is rapidly and mainly converted to CO resulting in almost unchanged selectivity profiles above 85 %. Again, in response to the applied feed variations of C_2H_4 and O_2, no change on selectivity in between the different profile runs is observable. The previous described results of the C_2H_4 measurement design are shown in supplementary material in Figure S9 and S10.

3.2.3 Variation in Temperature

Figure 8 and Figure 9 present the effect of an increasing reaction temperature on reactant consumption and (by)-product formation. Spatial profiling demonstrates well the expected impact of this variable over the rate of consumption/production of all species. Figure 8 shows in molar flow rates, that higher reaction temperatures enhance reactant consumption of C_2H_6 and

O_2 (a-b), while increasing the production of the target compound C_2H_4 (c) as well as side (d) and undesired (e,f) products.

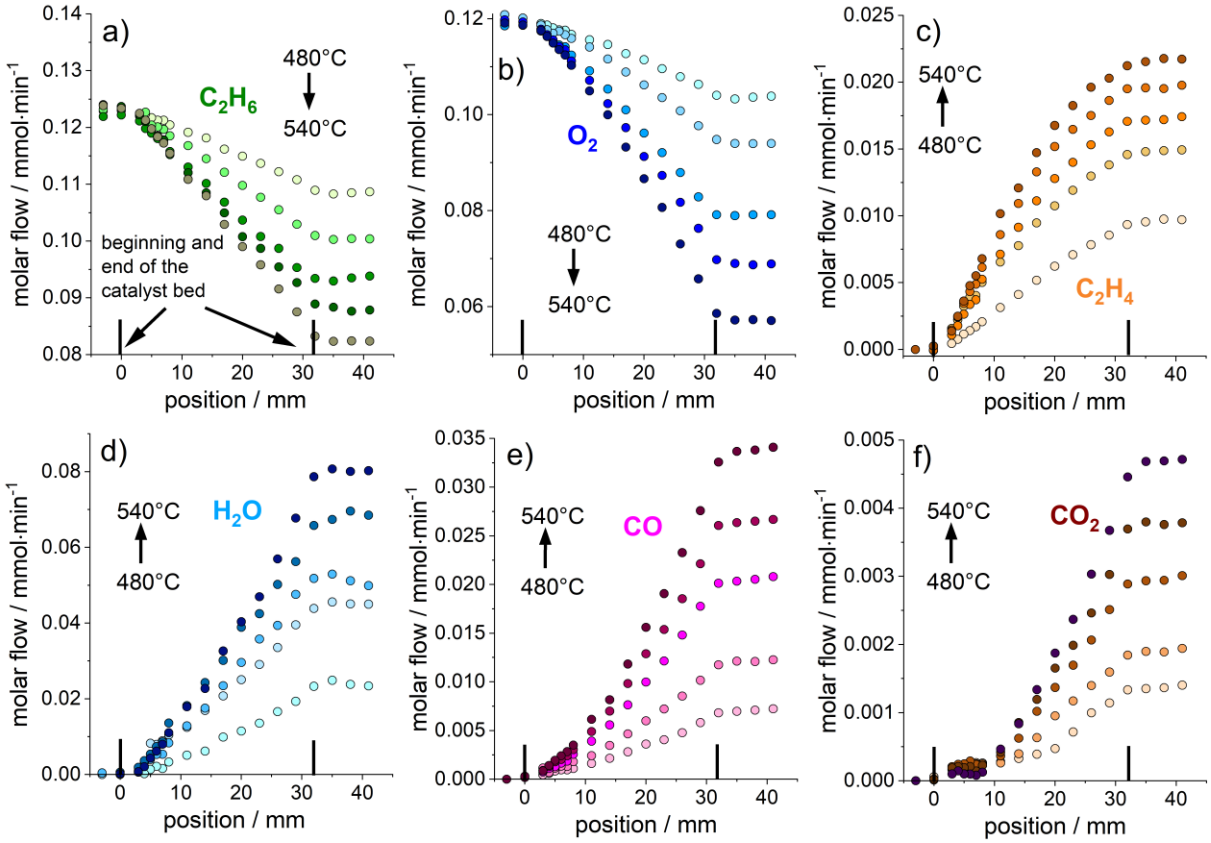

Figure 8: Species concentration profiles for all components measured at 480 (T13a), 500 (T13b), 520 (T13c), 530 (P13) and 540 °C (T13d) obtained in the C_2H_6 measurement plan. Reaction conditions: C_2H_6/O_2:10:10, 1 bar, 32 mm catalyst bed, 30 ml/min, 30 wt% MoO_3/γ-Al_2O_3.

In addition, Figure 9 shows the corresponding conversion profiles of C_2H_6 (a) and O_2 (b) as well as selectivity profiles of C_2H_4 (c), CO (d) and CO_2 (e). Selectivity profiles reveal clearly the effect of reaction temperature on product selectivity. Ethylene selectivities decrease strongly with higher temperatures (c), while selectivities of CO_x increase (d, e). As already discussed in Section 3.2.1, the shape of selectivity profiles is disturbed in the beginning of the catalyst bed due to an analytical artifact. A linear regression analysis at positions above 10 mm allows to estimate the expected selectivity at zero contact time. By using this methodology, product selectivities of CO, CO_2 and C_2H_4 add up to approximately 100 % at the inlet of the catalyst bed. Furthermore, Figure 9f shows the corresponding temperature profiles from 480-540 °C.

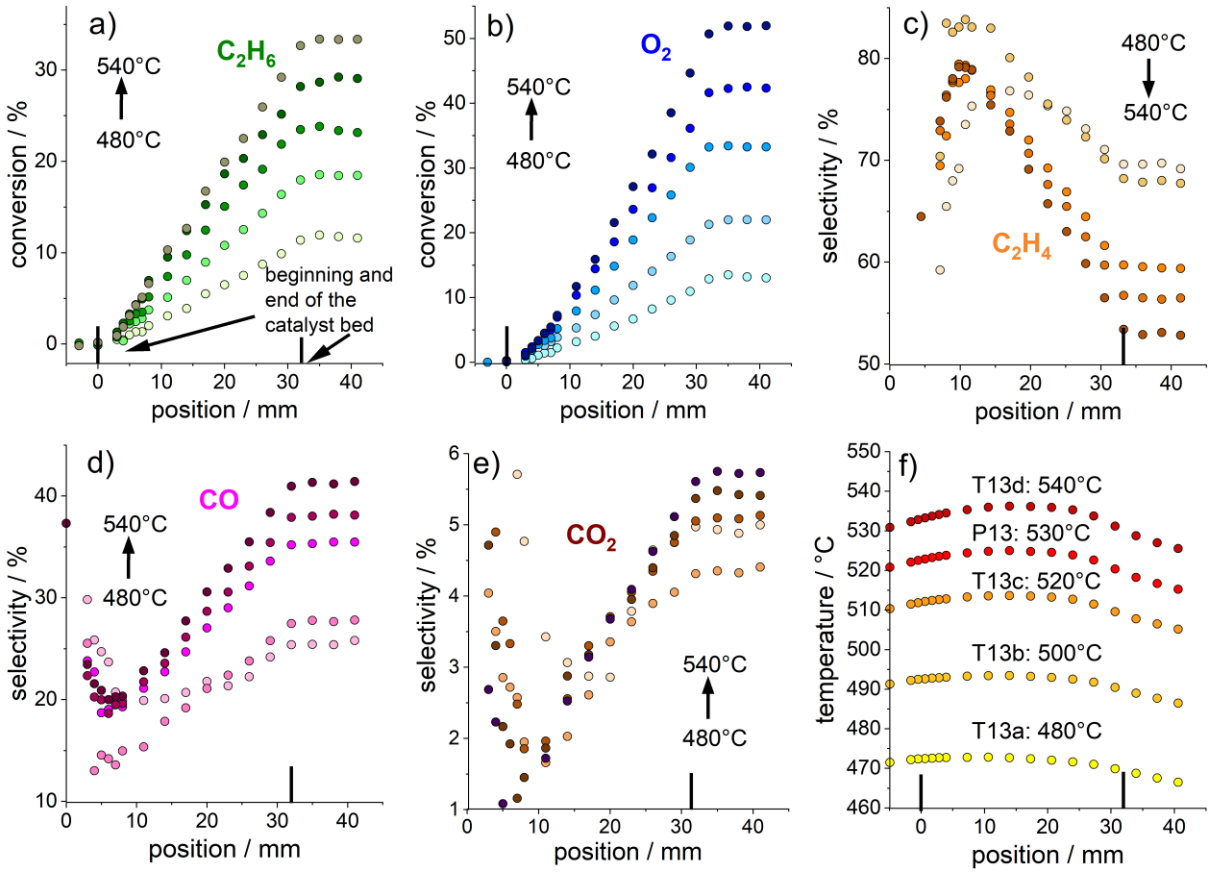

Figure 9: C_2H_6 (a), O_2 (b) conversion profiles and C_2H_4 (c), CO (d), CO_2 (e) selectivity profiles measured at 480 (T13a), 500 (T13b), 520 (T13c), 530 (P13) and 540 °C (T13d) (f) obtained in the C_2H_6 measurement plan. Reaction conditions: C_2H_6/O_2:10:10, 1 bar, 32 mm catalyst bed, 30 ml/min, 30 wt% MoO_3/γ-Al_2O_3.

Similar observations are made in feeding C_2H_4 and varying reaction temperatures (Figure S11). As described previously in Section 3.2.2, CO is produced with selectivities higher than 85 %. Reaction temperature shows only minor effect on changing reaction rates towards CO_2 (Figure S12).

3.2.4 Mars-van Krevelen Model

Since it is well established in research of ODH that reactions over transition metal oxides proceed usually by the MVK mechanism, it is used to macroscopically model the chemical system under investigation. The experimental data obtained in the catalyst activity studies served as basis to develop the kinetic model. Experiments were performed solely in the presence of gas phase oxygen up to 60% oxygen conversion. Therefore, the kinetic model includes only reactions with gas phase oxygen (Table 2). Furthermore, the goal is to derive a rate law that describes the observed data as simple as possible. For this, it is of central importance that the reactor is in steady state, because then all reaction steps have to be in steady state. Stable and reproducible operation within the time of the measurement campaign was observed (Figure 5). Figure 10a-c) shows the modeled and the measured concentration profiles (P13) for all species at 530 °C and C_2H_6/O_2:10/10. Visual inspection of the results suggests that the fitting procedure was successful throughout all species except of CO_2. An evaluation of the goodness of fit was addressed by parity plots and calculating the mean absolute percentage error (MAPE). Results are shown in Figure S13.

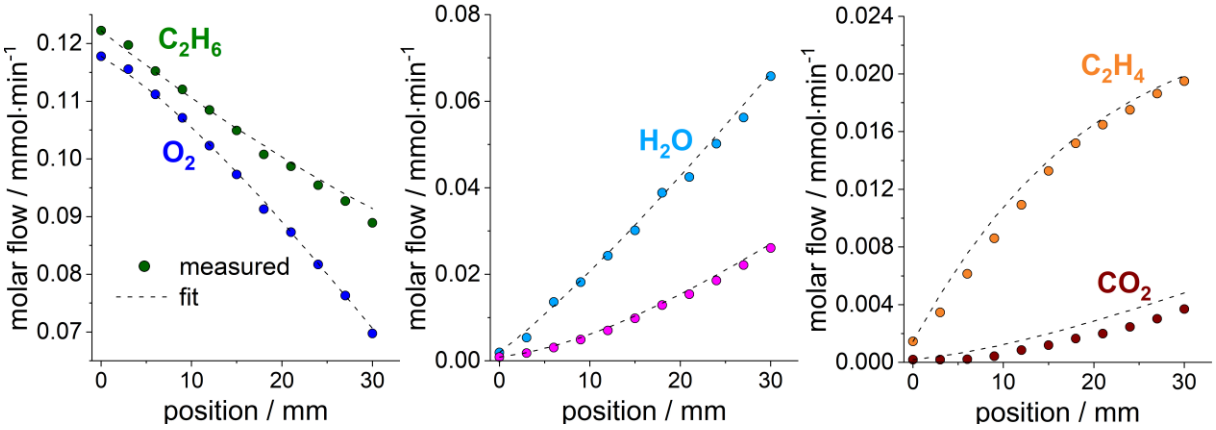

Figure 10: Measured species profiles of all components (P13) and the corresponding modeling results are shown. Reaction conditions: C_2H_6/O_2:10/10, 530°C, 1 bar, 32 mm catalyst bed, 30 ml/min, 30 wt% MoO_3/γ-Al_2O_3.

Table 2 shows the results of the kinetic model parameters obtained from the fitting process. The main reaction of ethane ODH shows an apparent activation energy of 102.4 kJ·mol^{-1}. The partial and total combustion of C_2H_6 towards CO and CO_2 show high activation energies of 117.9 kJ·mol^{-1} and 123.3 kJ·mol^{-1}. Lower activation energies of the entire reaction network are related to ethylene side reactions and the reoxidation of the catalyst. The relative low energy barrier determined for the reoxidation step of the catalyst structure suggests that this step is not rate determining, indicating that the structure is able to rapidly provide and incorporate oxygen. An analysis of the magnitude of reaction rates involved in the process indicates that indeed the reoxidation of the catalyst (r_6) is the fastest process in the whole proposed reaction scheme (Figure 11a). Previous results supporting this idea have been reported as it is in the case of Ressler et al. [46] who determined that reduction and reoxidation of MoO_x proceeds rapidly (solid state reaction is in the same order as gas phase reactions) at temperatures in the range of 773 K.

With regard to side reactions, the partial oxidation of ethylene requires 53.6 kJ·mol^{-1} while the energy required for total combustion is 88.8 kJ·mol^{-1}. These estimated values seem to be in agreement with profile observations shown in the previous Section 3.2.2. A comparison of activation energies and reparametrized exponential factors of individual reaction pathways that produce CO_x from HCs suggests that ethylene is the main contributor towards carbon monoxide in the range of operation conditions evaluated. This observation is congruent with results of previous studies where only minor parallel formation of carbon oxides coming from ethane was reported [37,47].

Table 2: Activation energies, reparametrized pre-exponential factors and oxygen reaction order, including their confidence intervals obtained via nonlinear least square method for the MVK model. Note that the reactions indicated do not represent elementary steps.

Reaction	Ea [kJ/mol]	Ao [mol/(kg s)]	n [-]
$C_2H_6 + O_l \xrightarrow{k1} C_2H_4 + H_2O + l$	102 ± 3	15.4E-03 ± 0.53E-03	-
$C_2H_6 + 5O_l \xrightarrow{k2} 2CO + 3H_2O + 5l$	118 ± 6	0.96E-03 ± 0.50E-03	-
$C_2H_6 + 7O_l \xrightarrow{k3} 2CO_2 + 3H_2O + 7l$	123 ± 6	0.31E-03 ± 0.34E-03	-
$C_2H_4 + 4O_l \xrightarrow{k4} 2CO + 2H_2O + 4l$	54 ± 2	50.9E-03 ± 5.66E-03	-
$C_2H_4 + 6O_l \xrightarrow{k5} 2CO_2 + 2H_2O + 6l$	89 ± 4	7.03E-03 ± 3.60E-03	-
$l + 0.5O_{2(g)} \xrightarrow{kox} O_l$	69 ± 3	248.0E-03 ± 40.50E-03	0.3 ± 0.04

Finally, in relation to the reaction order of oxygen involved in the reoxidation of the catalyst, a value of 0.3 was obtained. Hence, in this model the amount of oxygen in the gas phase has indeed a minor effect on the rate of reoxidation of the catalyst. A closer look at the magnitude of the kinetic parameters involved in this reaction step indicates that the process of providing oxygen through the catalyst is fast in comparison to other steps in the reaction mechanism.

The observations suggest that C_2H_6 consumption rate has a low reaction order with respect to O_2 concentration. An evaluation of the reaction order of O_2 as a function of its molar fraction, by using Eq.(9), is presented in Figure 11b.

$$n_{o2} = y_{o2} \frac{\partial \ln r_{net\ C_2H_6}}{\partial y_{o2}} \tag{9}$$

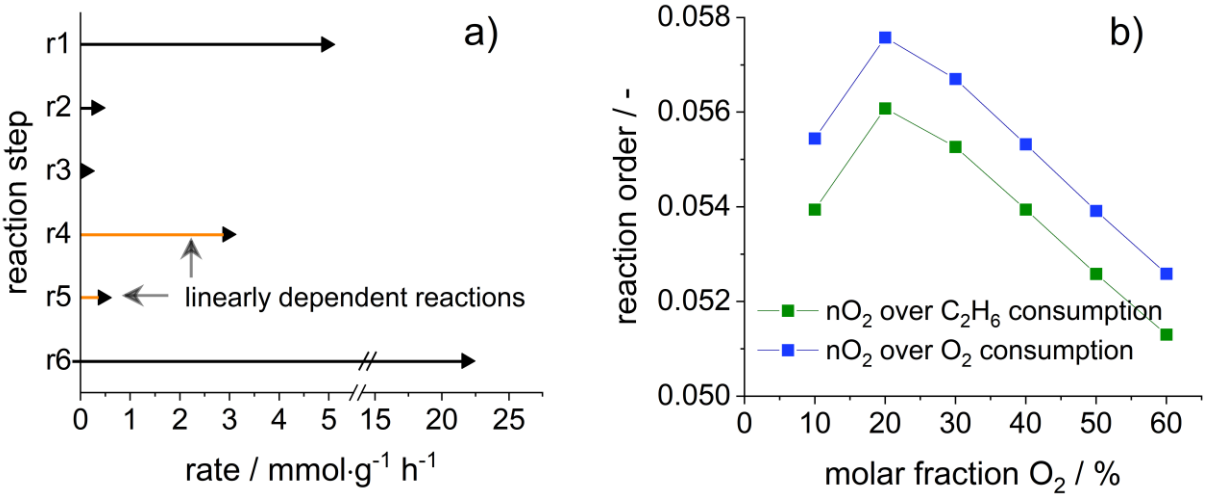

Figure 11: Evaluation of the rate determining step in the proposed MVK reaction scheme (a) and oxygen reaction order over ethane and oxygen consumption rate (b).

Spatially resolved measurement data provide insights into the reaction mechanism immediately upon application as shown in the example above. Initial consumption/production rates can be easily obtained from a simple linear regression analysis of the profiles at zero contact time. In combination with a reliable gas analytic system, this feature can be easily used to obtain experimental estimations of apparent activation energies as well as primary and secondary product formations. In a typical kinetic study setup under differential conditions, eleven parallel reactors would be needed in order to be able to reproduce one of the profiles obtained using the spatial profile measurement technique with the CPR. This advantage makes it possible to propose a kinetic model in a relatively short time interval (two weeks) and to reduce the required amount of experimental work heavily.

However, the results presented so far are only derived from gas phase analysis. Thus, information obtained are limited to a macroscopic understanding of the catalytic system under steady state conditions. Further knowledge about the catalyst itself apart from the percentage of oxidized sites remains unknown. Operando studies were performed to address the catalyst structure simultaneously.

3.3 Operando Study

3.3.1 Spatial Concentration Profiles

In Figure 12 species concentration profiles measured simultaneously with the XANES/EXAFS profile at the Mo K-edge through the 10 wt% MoO_3/ γ-Al_2O_3 catalyst bed are presented.

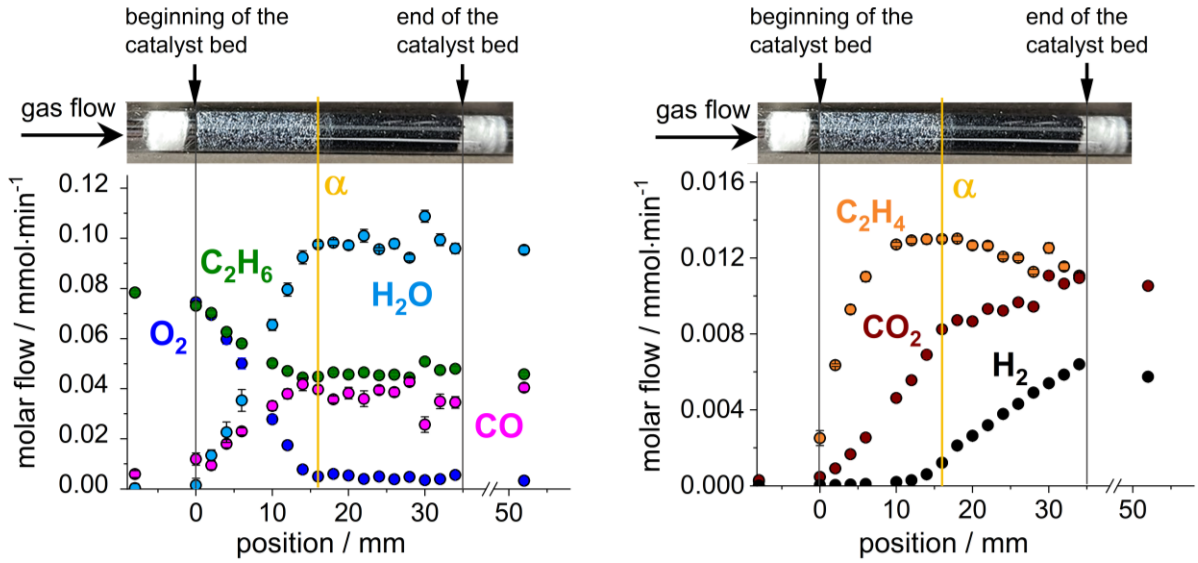

Figure 12: Species concentration profiles measured simultaneously with the XANES/EXAFS profile. Reaction conditions: C_2H_6/O_2:10/10, 530°C, 1 bar, 35 mm catalyst bed, 20 ml/min, 10 wt% MoO_3/γ-Al_2O_3. The sample is mounted vertically during the measurements.

The reaction mixture is composed of the feed components C_2H_6 and O_2, the main products C_2H_4 and H_2O as well as the undesired carbon oxides CO and CO_2. Measurements performed under ethane ODH conditions over MoO_3/γ-Al_2O_3 have common characteristics and compare well with the spatial concentration profiles presented in Section 3.2.2 (under oxidative conditions) as well as with a spatial profile study described in literature [37].

Ethane is readily oxidized to CO until 16 mm (labelled alpha). This point corresponds to a gas phase oxygen partial pressure of 6 mbar, indicating virtually complete oxygen consumption compared to the initial value of 94 mbar. In the presence of gas phase oxygen (i.e. from 0-16 mm along the bed) the main reaction products are H_2O, CO, CO_2 and C_2H_4. The latter shows a maximum in the profile that results from the plateau in C_2H_4 formation (from 10 mm bed position on) combined with further consumption. The maximum overlaps in position with complete oxygen conversion, onset of hydrogen formation and color inflection of the catalyst, denoted as alpha in Figure 12. In the absence of gas phase oxygen (i.e. from 16-35 mm along the bed) CO_2 and H_2 profiles increase towards the end of the catalyst bed. Since CO and H_2O concentration profiles are calculated from species balance und sum up measurement errors contributing from all other species, very small changes in H_2O and CO are difficult to evaluate. The change in color indicates that MoO_3 is reduced to MoO_2. This in turn creates a different phase composition with different catalytic properties. As example, MoO_2 has metallic properties. According to literature, MoO_2 is suitable to catalyze steam reforming as well as water-gas shift reactions [48]. This is in agreement to our species profile observations described above.

In conclusion, at low oxygen partial pressure the overall reaction mechanism changed and the catalyst adapted dynamically to the new gas composition, showing a change in color to black. Operando XAS measurements were simultaneously performed during profile measurements, to unravel the changes in catalyst structure observed around the inflection point and to complement the mechanistic investigation in the kinetic study.

3.3.2 Spatial Spectroscopic Profile

XANES

The catalyst sees strongly varying gas compositions along the flow direction. The previous Section 3.3.1 showed that the reaction mechanism changed as oxygen partial pressure declined to a lower limit. The gas concentrations illustrate only one part of the chemical system. The question arises how the catalyst adapted to the changing local conditions, which is focus of the following section.

Seventeen XANES/EXAFS spectra at the Mo K-edge were recorded under ODH reaction conditions through a 35 mm long and 4.8 mm thick catalyst bed. The spectra were taken at the same positions as the sampling points of the species concentration profiles discussed in the previous Section 3.3.1. Figure 13 shows the normalized Mo K-edge XANES spectra measured as function of position (a) and a linear combination analysis revealing the bulk Mo average oxidation state (b). Noticeable is the sharp decrease in the average Mo oxidation state at position 16 mm (α), whereas the spectra before and after this position are almost constant.

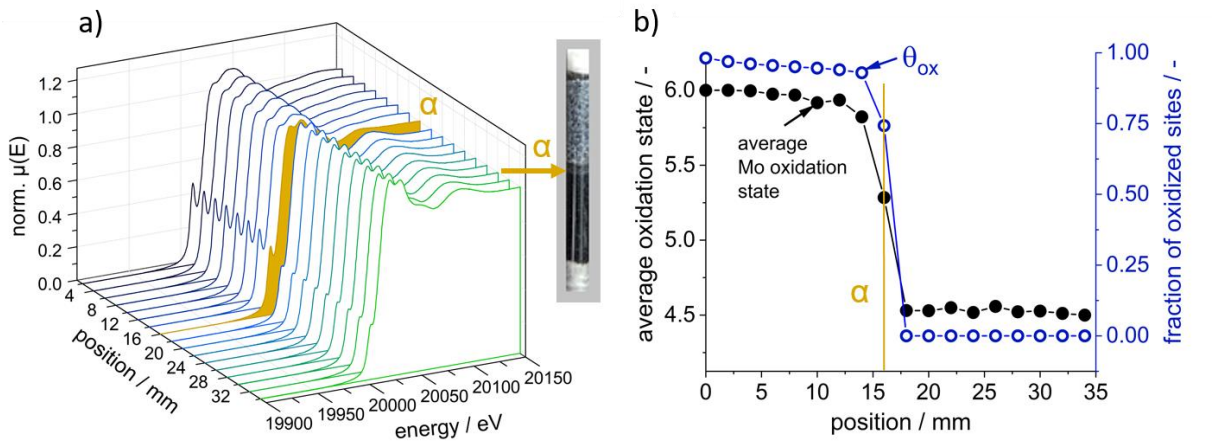

Figure 13: Operando XANES measurement at the Mo K-edge. a) Normalized XANES spectra as a function of the catalyst bed position; b) Linear combination analysis using spectra at the beginning (2 mm) and end (34 mm) of the catalyst bed as internal references and fraction of oxidized sites over catalyst surface obtained from the kinetic model. Reaction conditions: C_2H_6/O_2:10/10, 530 °C, 1 bar, 35 mm catalyst bed, 20 ml/min, 10 wt% MoO_3/γ-Al_2O_3.

To evaluate average oxidation states from the measured XANES profile, orthorhombic MoO_3 and monoclinic MoO_2 corresponding to Mo(VI) and Mo(IV) were used as references. In Figure 14a the sample spectra at position 2 mm and position 34 mm as well as the bulk MoO_3 and MoO_2 reference spectra are shown. The discrepancy between the reference spectra and sample spectra reveals a different structure of the supported MoO_x species relative to the bulk reference compounds. The spectrum measured at 2 mm is identical to the one of the calcined catalyst (not shown) and shows the same features and the same energy position E_0, allowing an assignment to Mo(VI) oxidation state. The spectrum at position 34 mm reveals the rising edge position and the white line shape (strongly absorbing feature(s) just above the rising edge) similar to the MoO_2 reference spectrum, however with a small contribution of an edge feature at 20006 eV as in the Mo(IV) spectra. To determine the exact oxidation state of this internal reference state the spectrum was fitted in the rising edge region (20008-20030 eV) to a linear combination of 2 mm (best available Mo(VI) reference) and the MoO_2 reference spectrum. This resulted in an average oxidation state of +4.5 at the end of the catalyst bed.

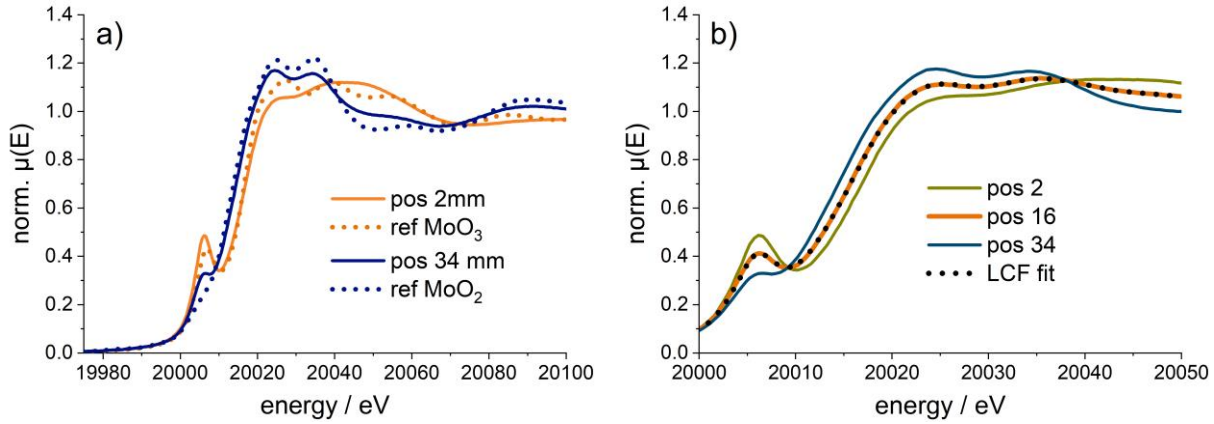

Figure 14: Normalized XANES spectra measured operando at Mo K-edge at the beginning (2mm) and end (34 mm) of the catalyst bed. a) Reference spectra of orthorhombic MoO_3 and monoclinic MoO_2 corresponding to Mo(VI) and Mo(IV) illustrated by dotted lines. b) Linear combination analysis of the spectrum at position 16 mm (position α, full oxygen conversion) between the spectra at position 2 and 34 mm.

The calcined catalyst changes its structure similar to monoclinic β-MoO_3 readily at the very beginning of the catalyst bed upon reaction as shown by a quick change in color from yellow to gray. The catalyst readily exchanges lattice with gas phase oxygen and provides lattice oxygen for ODH reactions [49]. Since optical properties of molybdenum oxides change strongly as a function of the oxygen vacancy concentration, the dark color results from induced oxygen defects in the catalyst material [50]. The oxygen vacancy concentration is thermodynamically determined by the oxygen partial pressure and increases with decreasing oxygen partial pressure [51,52]. Thus, MoO_3 is reduced to a certain degree in response to the local gas phase composition and temperature.

Although the oxygen partial pressure declines rapidly until position 16 mm (**α**), the average bulk oxidation state of Mo remains almost unchanged. This indicates that only a low concentration of oxygen vacancies is formed in the deep bulk. Reduction and reoxidation are obviously restricted to a near surface region. It has been speculated in literature that one of the well-defined molybdenum suboxides constitutes the active phase in ODH [53]. The slight decrease in the average Mo oxidation state before position 16 mm could also be explained by gradual reduction of a molybdenum suboxide phase present.

Below a certain oxygen partial pressure, the structure cannot compensate oxygen vacancies anymore and structural changes are induced rapidly, occurring in between position 14 and 18 mm. Linear combinations of spectra at the beginning (2 mm) and end of the catalyst bed (34 mm) show that the spectrum at position 16 mm can be created by mixing of the two. Therefore, position 16 mm is a weighted average of the two. Consequently, two isosbestic points arise, illustrated in Figure 14b. This shows that no stable or new intermediate phase can be detected with XANES.

The increasing oxygen vacancy concentration in steady state at each position with the declining gas phase oxygen concentration could lead to the formation of different suboxides like $Mo_{18}O_{52}$, Mo_8O_{23}, Mo_5O_{14} and Mo_4O_{11}, that have average oxidation states around 5.6-5.8 [54]. The formation of only near-stoichiometric MoO_{3-x} (x close to 0) compounds could compensate for oxygen vacancies in the bulk. According to Ressler et al. [54] applied reaction temperatures above 700 K make the participation of a considerable amount of lattice oxygen feasible. In combination with a rapid formation and growth of MoO_2 nuclei, a fast and complete transition of MoO_3 into MoO_2 occurs, as can be seen in the present data as well. Beyond alpha, the catalyst possesses a dark blue color, characteristic for MoO_2, that turned even darker towards the end of the bed. The average Mo oxidation state stabilizes close to Mo(IV).

Thermal treatment of MoO_3 under low oxygen partial pressures induces oxygen defects. In contrast, a phase diagram developed in the studies of Lee et al. [45] illustrates stable bulk molybdenum oxide phases as a function of temperature and partial pressure of oxygen. The current operando study was performed above 800 K and oxygen depletion follows a zeroth order. In addition, the presence of lower alkanes increases the reductive potential of the gas phase resulting in even more oxygen vacancies. Thus, the catalyst went quickly through the formation of MoO_3 to MoO_2. An increased sampling point density could have made the detection of a stable intermediate phase possible.

EXAFS

Fourier transformed (FT) k^2-weighted EXAFS functions and the corresponding fits for probed positions at 2 and 34 mm are shown in Figure S14 in the supplementary material. Backscattering peaks corresponding to the first shell in both operando EXAFS spectra are similar to the first shell peaks in the spectra of bulk reference compounds. However, virtually no further shells can be observed which suggests a lack of long range ordering for the MoO_X active species. The corresponding fitting parameters are listed in Table 3. Position 16 mm is again a perfect linear combination of the two spectra at the beginning and end of the catalyst bed and therefore, not separately discussed.

EXAFS revealed bond distances of three Mo-O paths 1.72±0.02 Å, 1.95±0.02 Å and 2.31±0.07 Å at position 2 mm. The sample is built of two to three MoO_4 distorted tetrahedra with an additional oxygen atom at a longer distance which can be considered as very strongly distorted octahedra. The structure found in the EXAFS refinement agrees well with structural XRD analysis performed by Kihlborg [55] and structural descriptions available [56].

Table 3: Amplitude reduction factor 0.95 obtained from fitting Mo foil reference spectrum. CN=coordination number, R=mean half-path length (interatomic distance for single scattering paths), σ^2=Debye-Waller factor, ΔE=fitted energy shift, ρ difference between the data and the fit.

Position	Path	CN	R, Å	σ^2, $10^{-3}\cdot Å^2$	ΔE, eV	ρ, %
2 mm	Mo-O	3.3±0.4	1.72±0.02	7.9±1.4	1.6±5.0	0.2
	Mo-O	0.8±0.9	1.95±0.02	7.9±1.4		
	Mo-O	0.6±0.6	2.31±0.07	7.9±1.4		
	Mo-O-O	20.9±13.4	3.00±0.07	5.8±13.1		
	Mo-Mo	2.0 (fixed)	3.22±0.03	23.6±5.6		
34 mm	Mo-O	2.7±0.3	2.02±0.01	3.8±1.4	12.5±1.5	2.1
	Mo-Mo	0.3±0.2	2.56±0.04	3.8±1.4		
	Mo-O	6.2±5.7	3.36±0.05	22.8±24.6		
	Mo-Mo	1.1±0.7	3.74±0.02	3.8±1.4		
	Mo-O-Mo	9.3±3.5	4.53±0.04	3.8±1.4		

The EXAFS region in the Mo K-edge spectra exhibited pronounced changes at position 16 mm (α), indicating the quick structural transformation as already observed in XANES spectra (Figure 13). The coordination number in the first shell decreases from 3.3 to 2.7 and the local structure around Mo abruptly changes to the one similar to MoO_2, reflecting structural transformation in agreement with the XANES data.

Operando spectroscopy provides one additional dimension of data revealing local and simultaneously measured information on catalyst properties. Obtained information agrees with catalytic performance studies as well as the kinetic model and complements it with mechanistic

understanding of underlying physico-chemical phenomena. This chemical understanding can be used to derive and tune models in a more efficient way, and also to validate them.

3.4 Conclusion

The limitations of spatially resolved operando XAS in heterogeneous catalysis were successfully pushed forward by development of the measurement concept used in this study. We introduce a profile reactor capable of measuring temperature, concentration and XAS profiles through a catalytic fixed-bed simultaneously and with high resolution. The advantages of the spatial profile reactor over contemporary setups, such as capillary microreactors, were shown by providing high-quality and informative data over short measurement campaigns. The major advantages include a fully automated system allowing uniform and industrially relevant reaction conditions, compatible with realistic sample geometry and many reaction systems, including condensable reactants. The use of synchrotron-based characterization techniques such as XAS significantly expands the characterization portfolio and can be extended to synchrotron XRD or small angle X-ray scattering techniques. Furthermore, the use of a standardized and highly reproducible reactor system improves the comparability of research studies from a technical perspective.

The spatially resolved structure-activity profiling concept was validated using ethane ODH to ethylene over a $MoO_3/\gamma\text{-}Al_2O_3$ catalyst. At the point of full gas phase oxygen depletion the catalyst changes optical properties, performance and structure, in comparison to the stable behavior shown before or after oxygen depletion. The change in color from yellow to grey at the catalyst bed inlet suggests a fast introduction of oxygen defects in the structure. This color remains stable until the sharp change in color from grey to dark blue/black occurred. At the same position localized kinetic measurements reveal a change in the reaction mechanism. The desired target product ethylene is not further produced, but instead consumed. In combination the *operando* spectroscopic XANES and EXAFS profile reveal a steep gradient in averaged Mo oxidation state from (VI) to (IV) as well as a change in structure from MoO_3 to MoO_2. However, the oxidation state and structure remain stable until very low oxygen partial pressures. Activation energies obtained in the kinetic model complete the observations by showing that the reoxidation of the catalyst is not the rate determining step. Thus, it can be concluded that the exchange between gas phase oxygen and catalyst is a fast process. The structure and the reaction mechanism do not change as long as oxygen can be refilled in the structure. Also the catalyst activity studies are congruent to this information, showing a low order kinetic behavior in oxygen, when evaluating ethane and ethylene rates of consumption. It suggests that the rate determining step must be related to ethane or ethylene activation. Regarding unwanted products, ethylene was found to mainly contribute to formation of carbon oxides in the presence of gas phase oxygen. Moreover, minor contributions from ethane towards CO_2 are predicted by the model. In the absence of gas phase oxygen, steam reforming and water-gas shift reactions contribute to the production of undesired carbon oxides. Overall, the observations support an MVK type mechanism.

The correlative and locally measured kinetic and spectroscopic data show highly complementary information. This demonstrates the strength of correlative catalyst structure-activity profiling in providing a clearer picture of the overall catalyst performance. Therefore, a strong motivation to extend the methodology to other spectroscopic methods as well as to examine a wide range of chemical reaction systems is encouraged. From a methodological point of view, spatial profiling demonstrates its power in reducing the experimental workload by half of the measurement time required in comparison to standard kinetic studies. Additionally, it increases the amount of spatially and temporally information used in the development of the model, since it does not follow the typical end-of-pipe approach used in traditional kinetic measurements. Thus, the applied methodology improves the predictive capability of the models. Here a kinetic model for ethane ODH over MoO_3 could be developed in two weeks and catalyst dynamics could be implemented in the model. This offers a great advantage in industrial applications as well as optimizing catalytic processes and catalysts in a more time and resource efficient way.

Acknowledgments

The authors thank Hamburg Innovation GmbH for funding the development of the profile reactor for operando X-Ray spectroscopy that was used in this work under the funding number C4T129. This work was supported by the German Federal Ministry of Education and Research (BMBF) project COSMIC (no. 05K19VK4). We acknowledge DESY (Hamburg, Germany), a member of the Helmholtz Association HGF, for the provision of experimental facilities. Parts of this research (XAS experiments) were carried out at beamline P64 (PETRA III) and the authors thank Wolfgang Caliebe and Marcel Görlitz for their support during the experiment. We are grateful to Christina Laarmann for producing $MoO_3/\gamma\text{-}Al_2O_3$ catalysts used in this study. We also thank F. Vrljic and B. Bevivino for the help during XAS measurements.

References

[1] B. Elvers, F. Ullmann (Eds.), Ullmann's encyclopedia of industrial chemistry, 7th ed., Wiley-VCH, Weinheim, 2011.

[2] T. Ren, M. Patel, K. Blok, Olefins from conventional and heavy feedstocks: Energy use in steam cracking and alternative processes, Energy 31 (2006) 425–451. https://doi.org/10.1016/j.energy.2005.04.001.

[3] T. Ren, M. Patel, K. Blok, Steam cracking and methane to olefins: Energy use, CO2 emissions and production costs, Energy (2008). https://doi.org/10.1016/j.energy.2008.01.002.

[4] W. Mackenzie, Ethylene Global Supply Demand Analytics Service, 2018. https://www.woodmac.com/news/editorial/ethylene-global-supply-demand-analytics-service/ (accessed 29 January 2021.634Z).

[5] F. Cavani, F. Trifirò, The oxidative dehydrogenation of ethane and propane as an alternative way for the production of light olefins, Catal. Today 24 (1995) 307–313. https://doi.org/10.1016/0920-5861(95)00051-G.

[6] F. Cavani, N. Ballarini, A. Cericola, Oxidative dehydrogenation of ethane and propane: How far from commercial implementation?, Catal. Today 127 (2007) 113–131. https://doi.org/10.1016/j.cattod.2007.05.009.

[7] F. Cavani, Catalytic selective oxidation: The forefront in the challenge for a more sustainable chemical industry, Catal. Today 157 (2010) 8–15. https://doi.org/10.1016/j.cattod.2010.02.072.

[8] J. Védrine, Heterogeneous Partial (amm)Oxidation and Oxidative Dehydrogenation Catalysis on Mixed Metal Oxides, Catalysts 6 (2016) 22. https://doi.org/10.3390/catal6020022.

[9] K. Morgan, J. Touitou, J.-S. Choi, C. Coney, C. Hardacre, J.A. Pihl, C.E. Stere, M.-Y. Kim, C. Stewart, A. Goguet, W.P. Partridge, Evolution and Enabling Capabilities of Spatially Resolved Techniques for the Characterization of Heterogeneously Catalyzed Reactions, ACS Catal. 6 (2016) 1356–1381. https://doi.org/10.1021/acscatal.5b02602.

[10] Y. Zhou, C. Jin, Y. Li, W. Shen, Dynamic behavior of metal nanoparticles for catalysis, Nano Today 20 (2018) 101–120. https://doi.org/10.1016/j.nantod.2018.04.005.

[11] M.A. Newton, Dynamic adsorbate/reaction induced structural change of supported metal nanoparticles: heterogeneous catalysis and beyond, Chem. Soc. Rev. 37 (2008) 2644–2657. https://doi.org/10.1039/b707746g.

[12] R. Schlögl, Heterogeneous catalysis, Angew. Chem., Int. Ed. 54 (2015) 3465–3520. https://doi.org/10.1002/anie.201410738.

[13] K.F. Kalz, R. Kraehnert, M. Dvoyashkin, R. Dittmeyer, R. Gläser, U. Krewer, K. Reuter, J.-D. Grunwaldt, Future Challenges in Heterogeneous Catalysis: Understanding Catalysts under Dynamic Reaction Conditions, ChemCatChem 9 (2017) 17–29. https://doi.org/10.1002/cctc.201600996.

[14] P. Kube, B. Frank, S. Wrabetz, J. Kröhnert, M. Hävecker, J. Velasco-Vélez, J. Noack, R. Schlögl, A. Trunschke, Functional Analysis of Catalysts for Lower Alkane Oxidation, ChemCatChem 9 (2017) 573–585. https://doi.org/10.1002/cctc.201601194.

[15] E. Heracleous, J. Vakros, A. Lemonidou, C. Kordulis, Role of preparation parameters on the structure–selectivity properties of MoO3/Al2O3 catalysts for the oxidative dehydrogenation of ethane, Catal. Today 91-92 (2004) 289–292. https://doi.org/10.1016/j.cattod.2004.03.046.
[16] S. Lwin, W. Diao, C. Baroi, A. Gaffney, R. Fushimi, Characterization of MoVTeNbOx Catalysts during Oxidation Reactions Using In Situ/Operando Techniques: A Review, Catalysts 7 (2017) 109. https://doi.org/10.3390/catal7040109.
[17] J. Le Bars, A. Auroux, M. Forissier, J.C. Vedrine, Active Sites of V2O5/γ-Al2O3Catalysts in the Oxidative Dehydrogenation of Ethane, J. Catal. 162 (1996) 250–259. https://doi.org/10.1006/jcat.1996.0282.
[18] J.M. López Nieto, J. Soler, P. Concepción, J. Herguido, M. Menéndez, J. Santamaría, Oxidative Dehydrogenation of Alkanes over V-based Catalysts: Influence of Redox Properties on Catalytic Performance, J. Catal. 185 (1999) 324–332. https://doi.org/10.1006/jcat.1999.2467.
[19] E.A. Mamedov, V. Cortés Corberán, Oxidative dehydrogenation of lower alkanes on vanadium oxide-based catalysts. The present state of the art and outlooks, Appl. Catal., A 127 (1995) 1–40. https://doi.org/10.1016/0926-860X(95)00056-9.
[20] J. Haber, Molecular mechanism of heterogeneous oxidation — organic and solid state chemists' views, in: R.K. Grasselli (Ed.), 3rd World Congress on Oxidation Catalysis: Proceedings of the 3rd World Congress on Oxidation Catalysis, San Diego, CA, U.S.A., 21-26 September 1997, Elsevier, Amsterdam, New York, 1997, pp. 1–17.
[21] J. Haber, Fundamentals of Hydrocarbon Oxidation, in: G. Ertl, H. Knözinger, F. Schüth, J. Weitkamp (Eds.), Handbook of heterogeneous catalysis, secondnd ed., Wiley-VCH, Weinheim, 2008, p. 465.
[22] R.K. Grasselli, Site isolation and phase cooperation: Two important concepts in selective oxidation catalysis: A retrospective, Catal. Today 238 (2014) 10–27. https://doi.org/10.1016/j.cattod.2014.05.036.
[23] H. Topsøe, Developments in operando studies and in situ characterization of heterogeneous catalysts, J. Catal. 216 (2003) 155–164. https://doi.org/10.1016/S0021-9517(02)00133-1.
[24] R. Horn, O. Korup, M. Geske, U. Zavyalova, I. Oprea, R. Schlögl, Reactor for in situ measurements of spatially resolved kinetic data in heterogeneous catalysis, Rev. Sci. Instrum. 81 (2010) 64102. https://doi.org/10.1063/1.3428727.
[25] J.-D. Grunwaldt, B. Kimmerle, A. Baiker, P. Boye, C.G. Schroer, P. Glatzel, C.N. Borca, F. Beckmann, Catalysts at work: From integral to spatially resolved X-ray absorption spectroscopy, Catal. Today 145 (2009) 267–278. https://doi.org/10.1016/j.cattod.2008.11.002.
[26] F. Meirer, B.M. Weckhuysen, Spatial and temporal exploration of heterogeneous catalysts with synchrotron radiation, Nat. Rev. Mater. 3 (2018) 324–340. https://doi.org/10.1038/s41578-018-0044-5.

[27] K.H. Cats, B.M. Weckhuysen, Combined Operando X-ray Diffraction/Raman Spectroscopy of Catalytic Solids in the Laboratory: The Co/TiO2 Fischer-Tropsch Synthesis Catalyst Showcase, ChemCatChem 8 (2016) 1531–1542. https://doi.org/10.1002/cctc.201600074.
[28] M.A. Bañares, Operando methodology: combination of in situ spectroscopy and simultaneous activity measurements under catalytic reaction conditions, Catal. Today 100 (2005) 71–77. https://doi.org/10.1016/j.cattod.2004.12.017.
[29] J.-D. Grunwaldt, S. Hannemann, C.G. Schroer, A. Baiker, 2D-mapping of the catalyst structure inside a catalytic microreactor at work: partial oxidation of methane over Rh/Al2O3, J. Phys. Chem. B 110 (2006) 8674–8680. https://doi.org/10.1021/jp060371n.
[30] J. Becher, D.F. Sanchez, D.E. Doronkin, D. Zengel, D.M. Meira, S. Pascarelli, J.-D. Grunwaldt, T.L. Sheppard, Chemical gradients in automotive Cu-SSZ-13 catalysts for NOx removal revealed by operando X-ray spectrotomography, Nat. Catal. 4 (2021) 46–53. https://doi.org/10.1038/s41929-020-00552-3.
[31] J.-D. Grunwaldt, M. Caravati, S. Hannemann, A. Baiker, X-ray absorption spectroscopy under reaction conditions: suitability of different reaction cells for combined catalyst characterization and time-resolved studies, Phys. Chem. Chem. Phys. 6 (2004) 3037. https://doi.org/10.1039/B403071K.
[32] Frederic C. Meunier, The design and testing of kinetically-appropriate operando spectroscopic cells for investigating heterogeneous catalytic reactions, Chem. Soc. Rev. 39 (2010) 4602–4614. https://doi.org/10.1039/B919705M.
[33] C. Stewart, E.K. Gibson, K. Morgan, G. Cibin, A.J. Dent, C. Hardacre, E.V. Kondratenko, V.A. Kondratenko, C. McManus, S. Rogers, C.E. Stere, S. Chansai, Y.-C. Wang, S.J. Haigh, P.P. Wells, A. Goguet, Unraveling the H2 Promotional Effect on Palladium-Catalyzed CO Oxidation Using a Combination of Temporally and Spatially Resolved Investigations, ACS Catal. 8 (2018) 8255–8262. https://doi.org/10.1021/acscatal.8b01509.
[34] D. Decarolis, A.H. Clark, T. Pellegrinelli, M. Nachtegaal, E.W. Lynch, C.R.A. Catlow, E.K. Gibson, A. Goguet, P.P. Wells, Spatial Profiling of a Pd/Al 2 O 3 Catalyst during Selective Ammonia Oxidation, ACS Catal. (2021) 2141–2149. https://doi.org/10.1021/acscatal.0c05356.
[35] J. Touitou, K. Morgan, R. Burch, C. Hardacre, A. Goguet, An in situ spatially resolved method to probe gas phase reactions through a fixed bed catalyst, Catal. Sci. Technol. 2 (2012) 1811. https://doi.org/10.1039/c2cy20141k.
[36] M.A. Newton, S. Checchia, A.J. Knorpp, D. Stoian, W. van Beek, H. Emerich, A. Longo, J.A. van Bokhoven, On isothermality in some commonly used plug flow reactors for X-ray based investigations of catalysts, Catal. Sci. Technol. 9 (2019) 3081–3089. https://doi.org/10.1039/C9CY00464E.
[37] M. Geske, O. Korup, R. Horn, Resolving kinetics and dynamics of a catalytic reaction inside a fixed bed reactor by combined kinetic and spectroscopic profiling, Catal. Sci. Technol. 3 (2013) 169–175. https://doi.org/10.1039/C2CY20489D.
[38] D.E. Mears, Diagnostic criteria for heat transport limitations in fixed bed reactors, J. Catal. 20 (1971) 127–131. https://doi.org/10.1016/0021-9517(71)90073-X.

[39] P. Mars, D.W. van Krevelen, Oxidations carried out by means of vanadium oxide catalysts, Chem. Eng. Sci. 3 (1954) 41–59. https://doi.org/10.1016/S0009-2509(54)80005-4.
[40] W.A. Caliebe, V. Murzin, A. Kalinko, M. Görlitz, High-flux XAFS-beamline P64 at PETRA III, Taipei, Taiwan, Author(s), 2019, p. 60031.
[41] B. Ravel, M. Newville, ATHENA, ARTEMIS, HEPHAESTUS: data analysis for X-ray absorption spectroscopy using IFEFFIT, J. Synchrotron Radiat. 12 (2005) 537–541. https://doi.org/10.1107/S0909049505012719.
[42] J.J. Rehr, R.C. Albers, Theoretical approaches to x-ray absorption fine structure, Rev. Mod. Phys. 72 (2000) 621–654. https://doi.org/10.1103/RevModPhys.72.621.
[43] M.C. Abello, M.F. Gomez, O. Ferretti, Catal. Lett. 87 (2003) 43–49. https://doi.org/10.1023/A:1022801126269.
[44] L. Seguin, M. Figlarz, R. Cavagnat, J.-C. Lassègues, Infrared and Raman spectra of MoO3 molybdenum trioxides and MoO3 · xH2O molybdenum trioxide hydrates, Spectrochim. Acta, Part A 51 (1995) 1323–1344. https://doi.org/10.1016/0584-8539(94)00247-9.
[45] Y.-J. Lee, T. Lee, A. Soon, Phase Stability Diagrams of Group 6 Magnéli Oxides and Their Implications for Photon-Assisted Applications, Chem. Mater. 31 (2019) 4282–4290. https://doi.org/10.1021/acs.chemmater.9b01430.
[46] T. Ressler, O. Timpe, T. Neisius, J. Find, G. Mestl, M. Dieterle, R. Schlögl, Time-Resolved XAS Investigation of the Reduction/Oxidation of MoO3−x, J. Catal. 191 (2000) 75–85. https://doi.org/10.1006/jcat.1999.2772.
[47] E. Heracleous, A.A. Lemonidou, Homogeneous and heterogeneous pathways of ethane oxidative and non-oxidative dehydrogenation studied by temperature-programmed reaction, Appl. Catal., A 269 (2004) 123–135. https://doi.org/10.1016/j.apcata.2004.04.007.
[48] A. Katrib, P. Leflaive, L. Hilaire, G. Maire, Molybdenum based catalysts. I. MoO2 as the active species in the reforming of hydrocarbons, Catal. Lett. 38 (1996) 95–99. https://doi.org/10.1007/BF00806906.
[49] E.A. Gulbransen, K.F. Andrew, F.A. Brassart, Oxidation of Molybdenum 550° to 1700°C, J. Electrochem. Soc. 110 (1963) 952. https://doi.org/10.1149/1.2425918.
[50] V.R. Porter, W.B. White, R. Roy, Optical spectra of the intermediate oxides of titanium, vanadium, molybdenum, and tungsten, J. Solid State Chem. 4 (1972) 250–254. https://doi.org/10.1016/0022-4596(72)90113-2.
[51] D. Wilmer, Chemical Kinetics of Solids. VonH. Schmalzried. VCH Verlagsgesellschaft, Weinheim, 1995. 433 S., geb. 298.00 DM. - ISBN 3-527-29094-X 6 und 7, Angew. Chem. 107 (1995) 2617–2618. https://doi.org/10.1002/ange.19951072131.
[52] P.L. Gai, E.D. Boyes, S. Helveg, P.L. Hansen, S. Giorgio, C.R. Henry, Atomic-Resolution Environmental Transmission Electron Microscopy for Probing Gas–Solid Reactions in Heterogeneous Catalysis, MRS Bull. 32 (2007) 1044–1050. https://doi.org/10.1557/mrs2007.214.
[53] T. Ressler, J. Wienold, R.E. Jentoft, F. Girgsdies, Evolution of Defects in the Bulk Structure of MoO3 During the Catalytic Oxidation of Propene, Eur. J. Inorg. Chem. 2003 (2003) 301–312. https://doi.org/10.1002/ejic.200390040.

[54] T. Ressler, Bulk Structural Investigation of the Reduction of MoO3 with Propene and the Oxidation of MoO2 with Oxygen, J. Catal. 210 (2002) 67–83. https://doi.org/10.1006/jcat.2002.3659.
[55] L. Kihlborg, The Crystal Chemistry of Molybdenum Oxides, in: R. Ward (Ed.), Non-stoichiometric Compounds, Am. Chem. Soc., Washington, D. C., 1963, pp. 37–45.
[56] I.A. de Castro, R.S. Datta, J.Z. Ou, A. Castellanos-Gomez, S. Sriram, T. Daeneke, K. Kalantar-Zadeh, Molybdenum Oxides - From Fundamentals to Functionality, Adv. Mater. 29 (2017). https://doi.org/10.1002/adma.201701619.

Supplementary

Exploring Catalyst Dynamics in a Fixed Bed Reactor by Correlative Operando Spatially-Resolved Structure-Activity Profiling

B. Wollak[a], D. E. Doronkin[b,c], D. Espinoza[a], T. Sheppard[b,c], O. Korup[a,d], M. Schmidt[d], S. Alizadefanaloo[f], F. Rosowski[e], C. Schroer[f,g], J.-D. Grunwaldt[b,c], R. Horn*[a,d]

* Corresponding author

[a] Hamburg University of Technology, Institute of Chemical Reaction Engineering, Eißendorfer Str. 38, 21073 Hamburg, Germany, E-Mail: horn@tuhh.de

[b] Karlsruhe Institute of Technology, Institute for Chemical Technology and Polymer Chemistry, Engesserstr. 18/20, 76131 Karlsruhe, Germany

[c] Karlsruhe Institute of Technology, Institute of Catalysis Research and Technology, Hermann-von-Helmholtz-Platz 1, 76344 Eggenstein-Leopoldshafen, Germany

[d] Reacnostics GmbH, Am Kaiserkai 30, 20457 Hamburg, Germany

[e] UniCat BASF Joint Lab, Hardenbergstraße 36, 10623 Berlin, Germany

[f] Deutsches Elektronen-Synchrotron DESY, Notkestraße 85, 22607 Hamburg, Germany

[g] Department Physik, Universität Hamburg, Luruper Chaussee 149, 22761 Hamburg, Germany

2 Experimental

2.4 Spatial Profile Studies

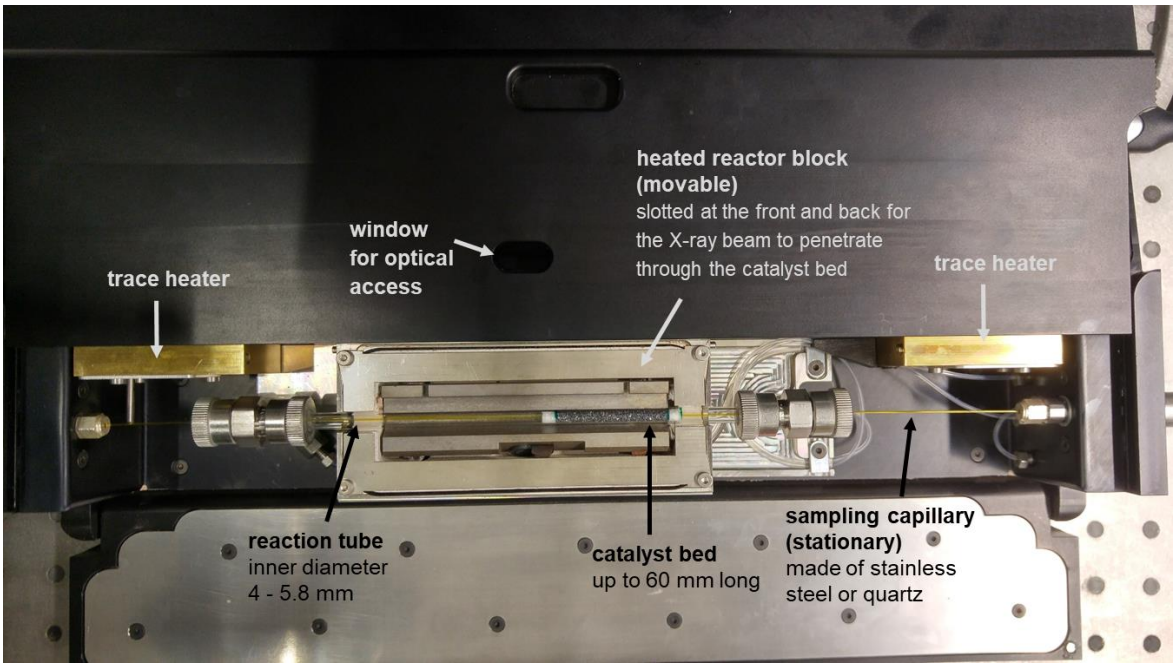

Figure S 1: Compact profile reactor used for combined operando concentration-, temperature- and XAS-profile measurements.

Supplementary

2.4.1 Catalyst Activity

Quantification via MS

Contributions were calculated from the fragmentation pattern of each of the involved component:

$$I_i = \sum_{j=1}^{n} S_i^c \; I^c \tag{S1}$$

Here I_i is the corrected signal intensity at mass i. S_i^c represents the contribution of species c to peak i and I^c is a non-overlapping signal of component c.

The previously listed species were calibrated with exception of water. Calibration experiments were done by sampling at reaction conditions. Volumetric flow rates were calculated by using the internal standard method (Ar):

$$\frac{I_c}{I_{IS}} = m_c * \frac{\dot{V_c}}{\dot{V_{IS}}} \tag{S2}$$

Where I_{IS} represents the signal intensity of the internal standard, m_c is the calibration slope, $\dot{V_c}$ and $\dot{V_{IS}}$ represent the volumetric flow rate of component c and internal standard, respectively.

Water was calculated from H atom species balance of the reaction mixture according to Eq.(S), where $\dot{n_{A,in}}$ and $\dot{n_{A,out}}$ represents the moles of atom A entering and leaving the system. By using this methodology carbon and oxygen balances for all profile runs were closed with average deviations of up to 5 %.

$$\sum \dot{n_{A,in}} - \sum \dot{n_{A,out}} = 0 \tag{S3}$$

To evaluate catalytic performance in all profile runs, conversion (X_i) was obtained by averaging the sampling points before and after the catalytic bed. This response parameters are calculated on basis of the molecular flow rates. Where $\dot{n_{i,o}}$ and $\dot{n_i}$ are the inlet and outlet molecular flows of reagent i (C_2H_6; O_2).

$$X_i(\%) = \frac{\dot{n_{i,o}} - \dot{n_i}}{\dot{n_{i,o}}} * 100 \tag{S4}$$

Selectivity of product k (C_2H_4; CO; CO_2) is determined:

$$S_k(\%) = \frac{m_k * \dot{F_k}}{\sum m_k * \dot{F_k}} * 100 \tag{S5}$$

Where $\dot{F_k}$ is the molecular flow of product k and m_k is the number of carbon atoms in species k respectively.

Transport limitations

Mass transfer limitations were evaluated by using the experimental rates of consumption of C_2H_6. The mass transfer coefficient was calculated by using the Thoenes and Kramers

correlation for flow through packed beds [1]. Diffusion coefficients where computed according to the kinetic theory of gases using the approach from Chapman-Enskog theory [2].

Weisz-Prater [3]: Intraparticle mass transport

$$\frac{\mathcal{R}_{rx}\, r_p^2}{C_s\ D_e} \leq 0{,}3 \tag{S6}$$

$\mathcal{R}_{rx}$: Observed reaction rate per unit particle volume [mol·m^{-3}·s^{-1}]
C_s: Reactant concentration at the external surface of the particle [mol·m^{-3}]
r_p: Particle radius [m]
D_e: Effective diffusion coefficient [m^2·s^{-1}]

Mears [3]: Interparticle mass transport

$$\frac{r_{v,obs}\, \rho_b\, r_p\, n}{k_c\ C_s} < 0{,}15 \tag{S7}$$

n: Reaction order [-]
ρ_b: Bulk density of catalyst bed [kg·m^{-3}]
k_c: Mass transfer coefficient [m·s^{-1}]

Potential heat transfer limitations were evaluated by assuming that only the main reaction, the oxidative dehydrogenation takes place, and that surface catalyst temperature is similar to the bulk gas temperature. The heat transfer coefficient was estimated according to literature [4].

Anderson [3]: Intraparticle heat transport

$$\frac{|\Delta H_r|\, r_{v,obs}\, \rho_b\, r_p^2}{\lambda\, T_s} < \frac{T_s\, R}{E_a} \tag{S8}$$

$|\Delta H_r|$: Heat of reaction [J·mol^{-1}]
λ: Thermal conductivity [W·m^{-1}·K^{-1}]
E_a: True activation energy [J·mol^{-1}]
R: Universal gas constant [J·mol^{-1}·K^{-1}]
T_s: Temperature of the catalyst surface [K]

Mears [3]: Interparticle heat transport

$$\frac{|\Delta H_r|\, r_{v,obs}\, \rho_b\, r_p}{h\, T_b} < 0.15 \frac{T_b\, R}{E_a} \tag{S9}$$

h: Heat transfer coefficient [W·m^{-2}·K^{-1}]
T_b: Temperature of the bulk fluid [K]

Mears [5]: Radial temperature gradient at reactor scale

Supplementary

Potential radial temperature gradients at reactor scale were evaluated by the criterion for minimal radial temperature profiles according to Mears. Only the main and strongly exothermic reaction of ethane ODH is considered to take place. For laboratory reactors that fulfill the criteria $Re_p < 100$ and $0.05 < d_p/d_t < 0.2$ the dimensionless Biot number at the wall is between $0{,}8 < Bi_{h,w} < 10$. A high Biot number of 10 is assumed to calculate for the case that the effective thermal conductivity of the bed is low and temperature gradients are more severe.

$$\frac{E_a}{RT_w}\left|\frac{r_{v,obs}(-\Delta H_r)d_t^2}{4\lambda_{b,eff}T_w}\right|\left(\frac{1}{8}+\frac{1}{Bi_{h,w}}\frac{d_p}{d_t}\right) < 0.05 \qquad \text{(S10)}$$

T_w: Temperature of the wall [K]
$r_{v,obs}$: Observed reaction rate per mass of catalyst [mol·kg^{-1}·s^{-1}]
$\lambda_{b,eff}$: Effective thermal conductivity [W·m^{-1}·K^{-1}]
$Bi_{h,w}$: Biot number at the wall [-]
d_p: Particle diameter [m]
d_t: Inner diameter of the reaction tube [m]

Table S 1: Overview of dimensionless criteria evaluated to test for the significance of intraparticle mass and heat transfer limitations as well as radial temperature gradient at reactor scale.

	Criteria	Value	Upper Limit
Intraparticle Mass Transport	Weisz and Prater	4.64E-03	0.3
Interparticle Mass transport	Mears	8.19E-03	0.15
Intraparticle Heat Transport	Anderson	6.52E-07	0.068
Interparticle Heat transport	Mears	1.97E-04	0.00987
Radial temperature gradient at reactor scale	Mears	1.56E10-06	0.05

2.4.3 Operando X-Ray Absorption Spectroscopy

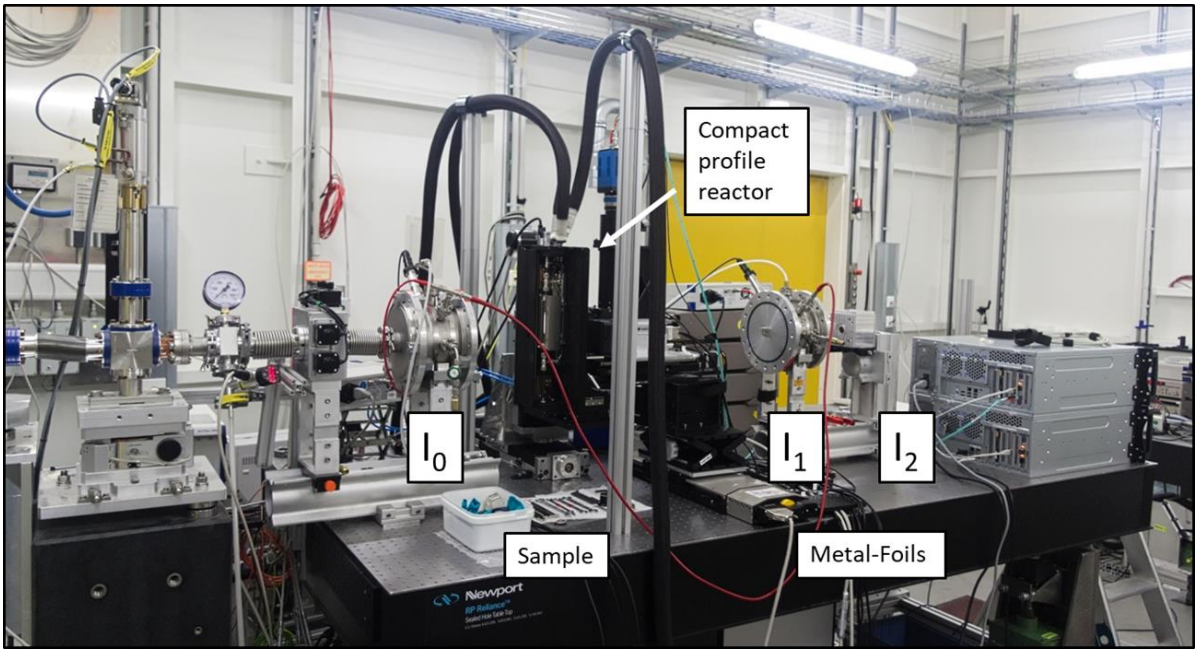

Figure S 2: Experimental setup used to obtain temperature, concentration and X-Ray absorption profiles using the compact profile reactor at beamline P64 at the PETRA III synchrotron radiation source (DESY, Hamburg, Germany).

3 Results and Discussion

3.1 Catalyst Characterization

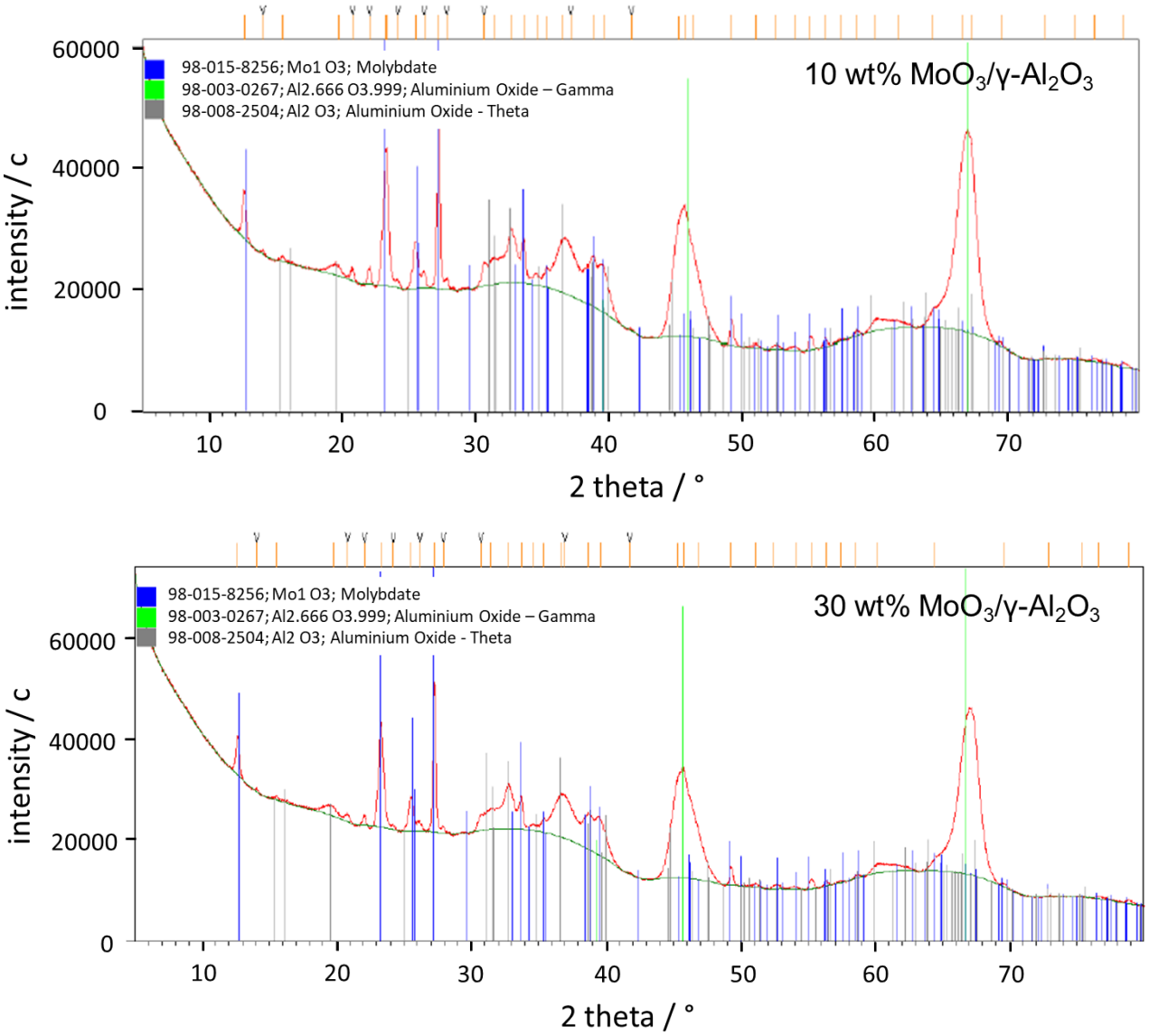

Figure S 3: X-ray diffraction patterns of the ex-situ analysis using the Kα lines of copper. Top: 10 wt% MoO_3/γ-Al_2O_3; Bottom: 30 wt% MoO_3/γ-Al_2O_3

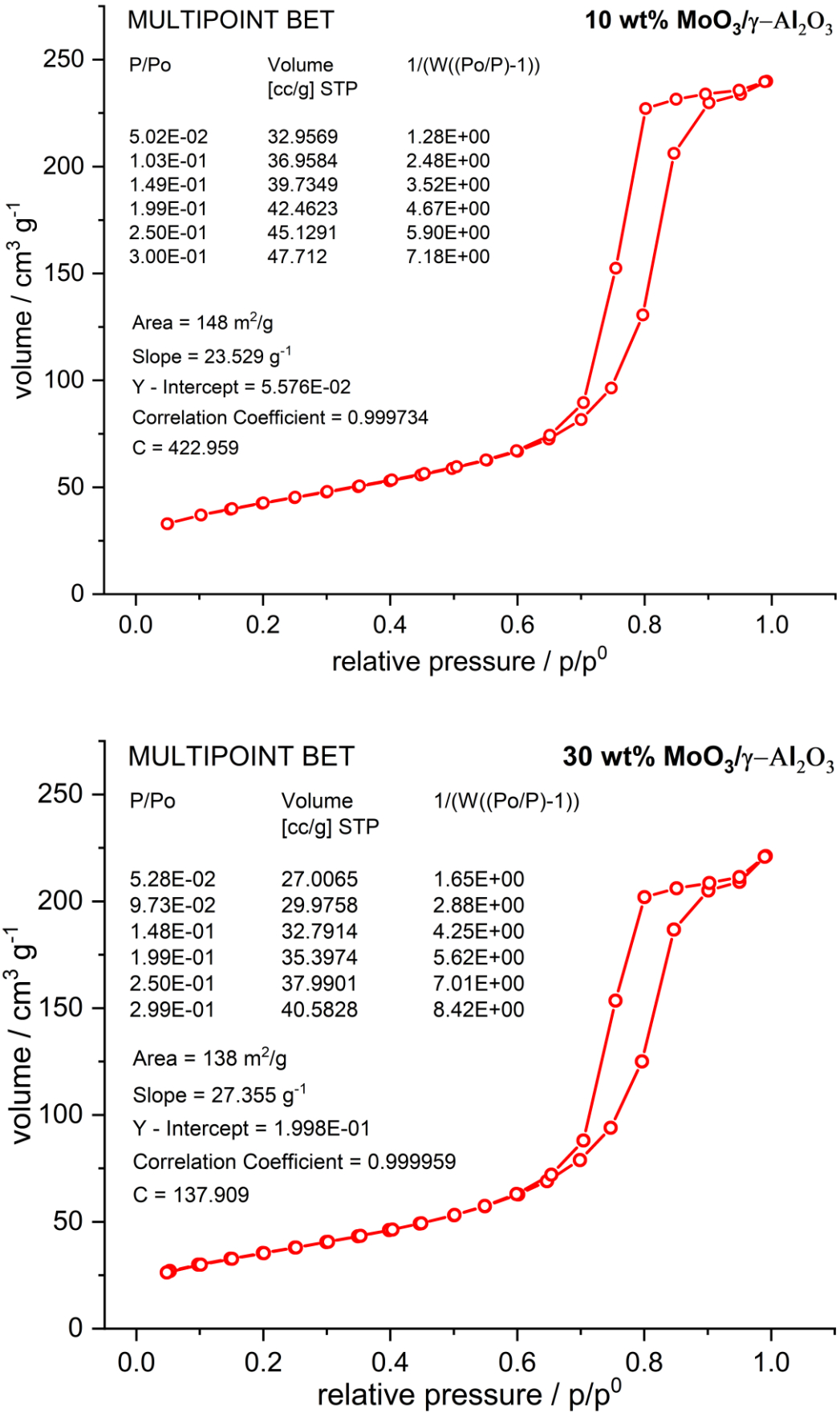

Figure S 4: Nitrogen adsorption-desorption isotherms (type IV). Top: 10 wt% MoO_3/γ-Al_2O_3; Bottom: 30 wt% MoO_3/γ-Al_2O_3.

3.2 Catalyst Activity Profiling

3.2.1 Stability and Reproducibility Tests

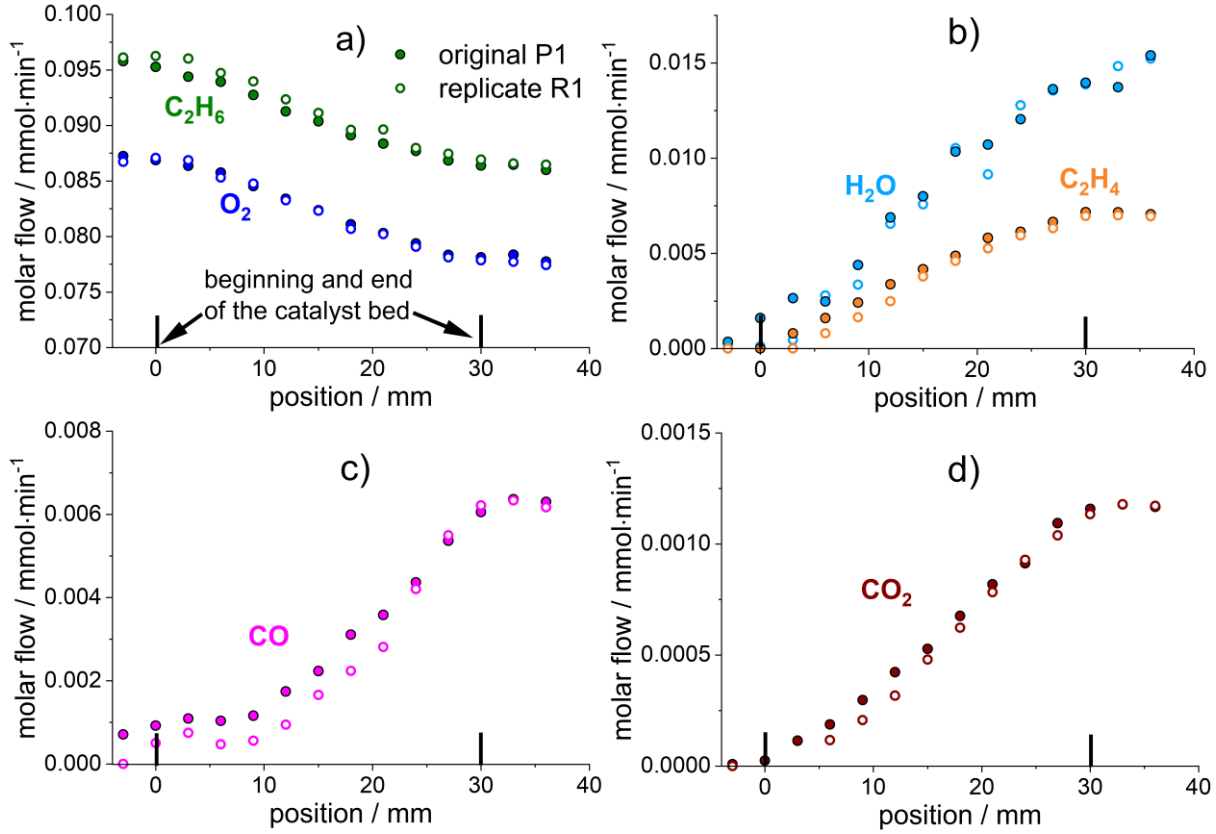

Figure S 5: Profile runs measured in the first measurement design plan are shown of the original profile (P1) and its replicate (R1a). a-d) Profiles of all species are shown in molar flow rates. Reaction conditions: C_2H_6/O_2:7.5:7.5, 480 °C, 1 bar, 30 mm catalyst bed, 30 ml/min, 30 wt% MoO_3/γ-Al_2O_3.

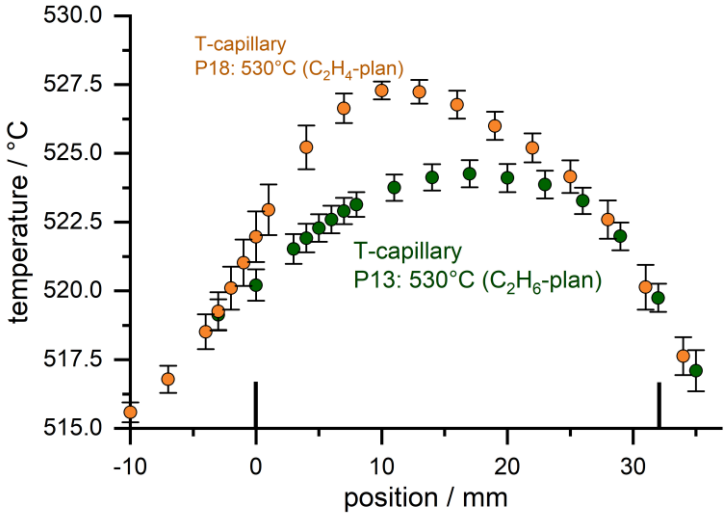

Figure S 6: (a) Averaged temperature profiles of the central point for the C_2H_6 (P13) and C_2H_4 (P18) measurement plan. Error bars are derived from the replicates by calculating the standard error. Reaction conditions: 530 °C, C_2H_6/O_2:10:10; C_2H_4/O_2:5:10, 1 bar, 32 mm catalyst bed, 30 ml/min (C_2H_6-plan), 40 ml/min (C_2H_4-plan), 30 wt% MoO_3/γ-Al_2O_3.

3.2.2 Variation in Feed Concentrations

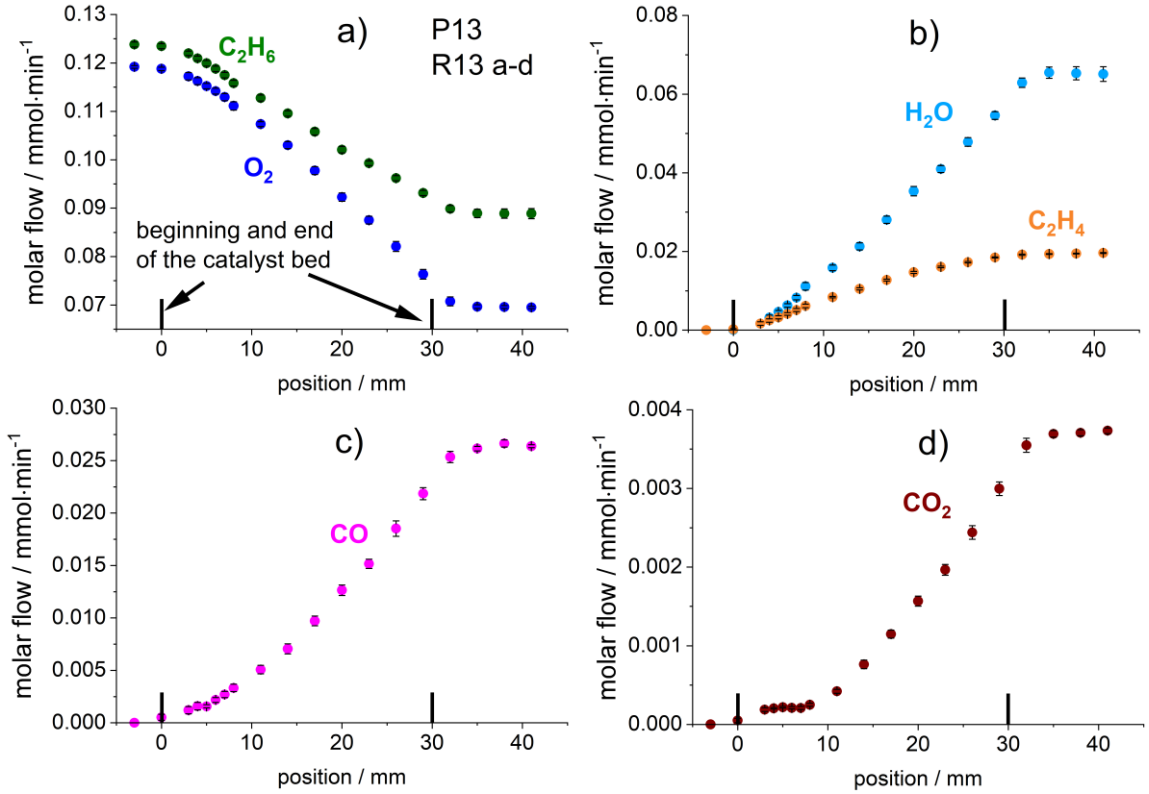

Figure S 7: Profile runs measured in the second measurement design plan are shown of the original profile (P13) with standard errors calculated from its replicates (R13a-d). Profiles of all species are shown in molar flow rates. Reaction conditions: C_2H_6/O_2:10:10, 530 °C, 1 bar, 32 mm catalyst bed, 30 ml/min, 30 wt% MoO_3/γ-Al_2O_3.

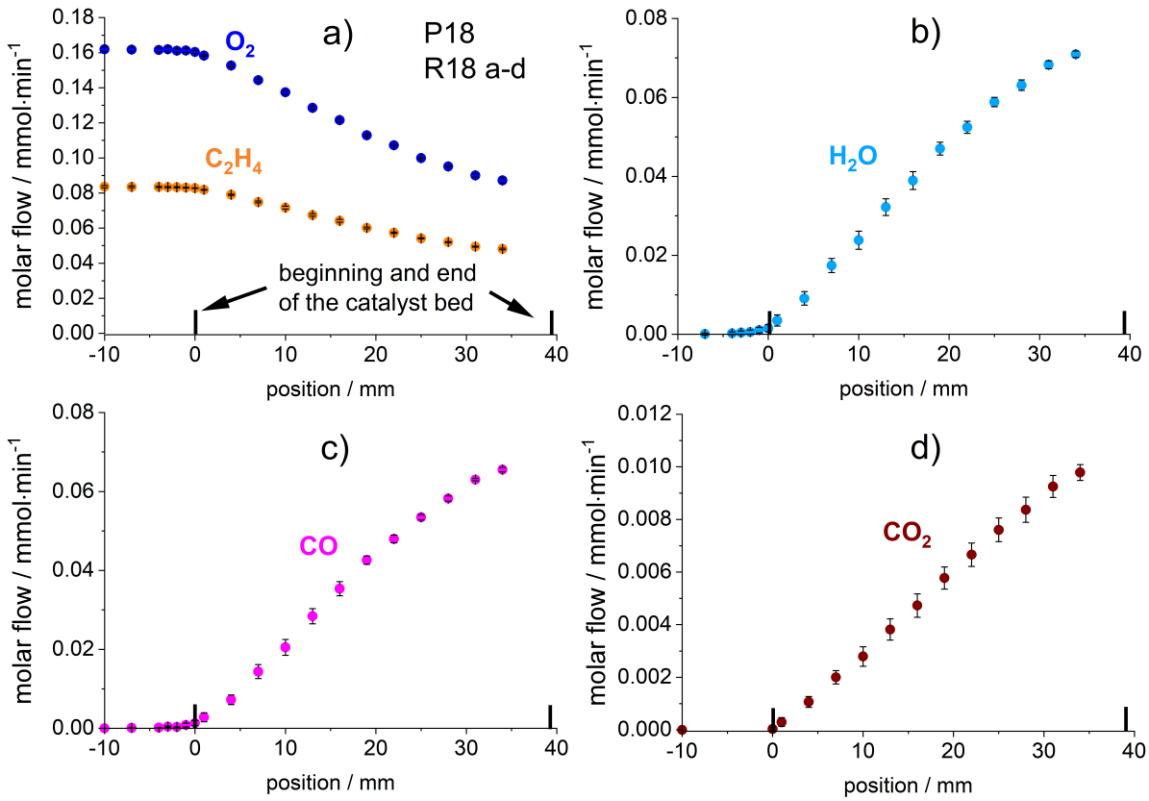

Figure S 8: Profile runs measured in the second measurement design plan of ethylene are shown of the original profile (P18) with standard errors calculated from its replicates (R18a-d). Profiles of all species are shown in molar flow rates. Reaction conditions: C_2H_4/O_2:5:10, 530 °C, 1 bar, 32 mm catalyst bed, 40 ml/min, 30 wt% MoO_3/γ-Al_2O_3.

Supplementary

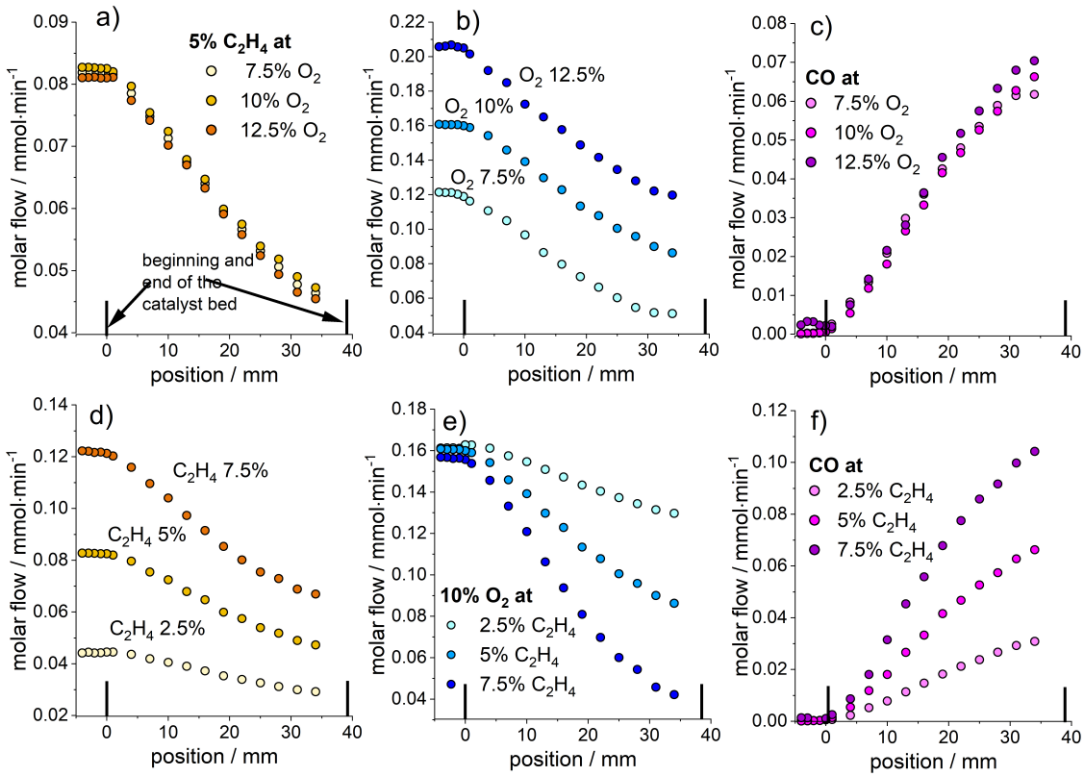

Figure S 9: Feed variations of O_2 (1st row) at reactant concentrations of 7.5, 10 and 12.5 % and C_2H_4 (2nd row) at reactant concentrations of 2.5, 5 and 7.5 % (P15, P17-19, P21). All percentage values are in a molar base. (a,d) C_2H_4; (b,e) O_2; (c,f) CO concentration profiles. Reaction conditions: 530°C, 1 bar, 32 mm catalyst bed, 40 ml/min, 30 wt% MoO_3/γ-Al_2O_3.

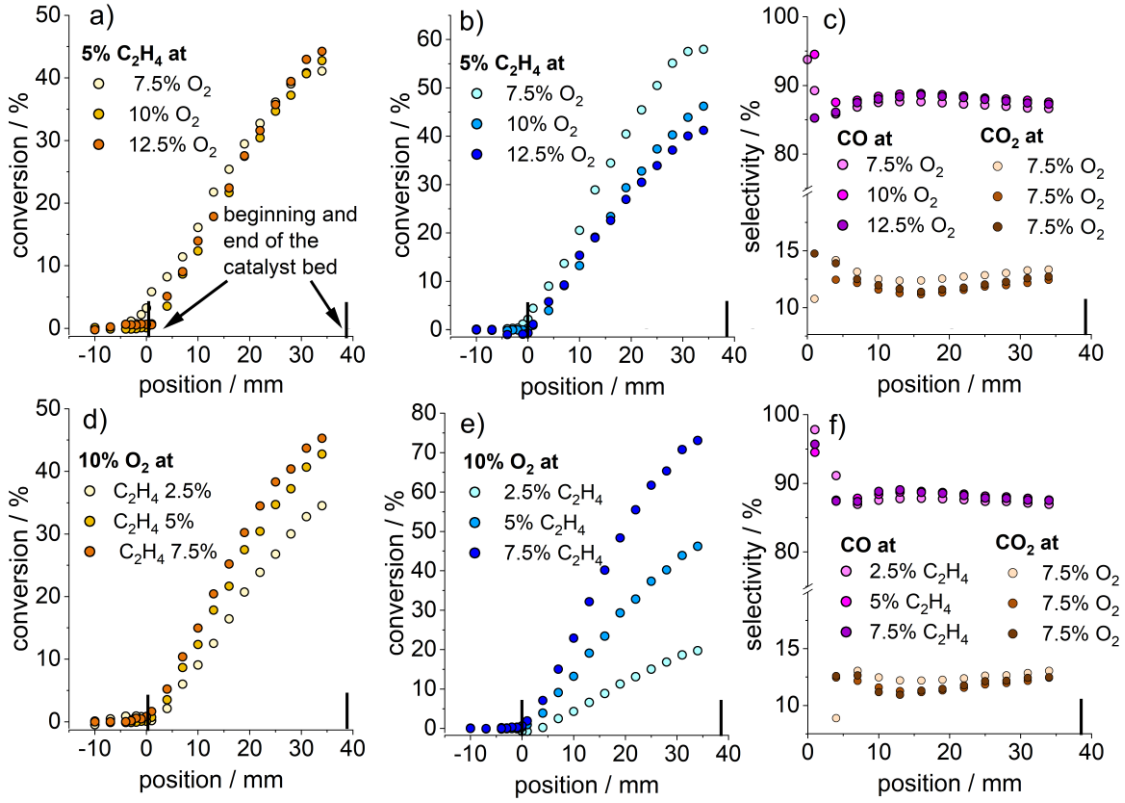

Figure S 10: Feed variations of O_2 (1st row) at reactant concentrations of 7.5, 10 and 12.5 % and C_2H_4 (2nd row) at reactant concentrations of 2.5, 5 and 7.5 % (P15, P17-19, P21). All percentage values are in a molar base. (a,d) C_2H_4; (b,e) O_2 conversion profiles. (c,f) CO selectivity profiles. Reaction conditions: 530°C, 1 bar, 32 mm catalyst bed, 40 ml/min, 30 wt% MoO_3/γ-Al_2O_3.

3.2.2 Variation in temperature

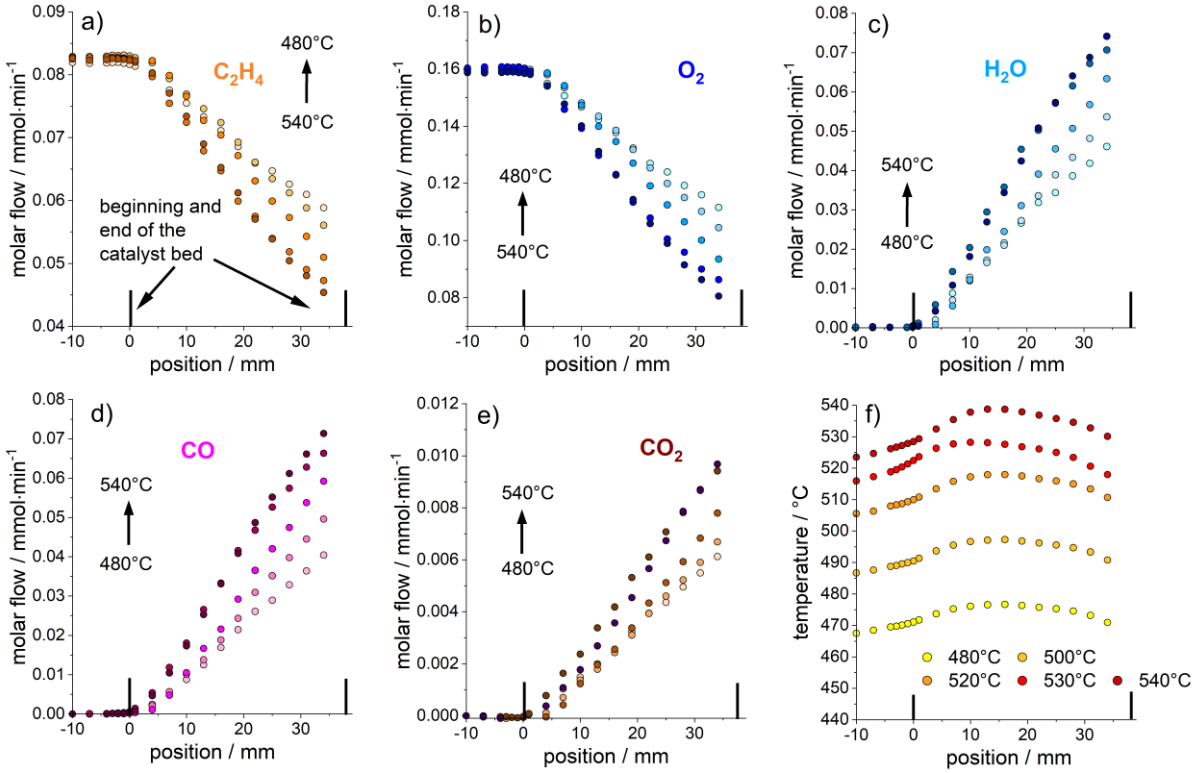

Figure S 11: Species concentration (a-e) and temperature profiles (f) for all components measured at 480 (T18a), 500 (18b), 520 (T18c), 530 (T18) and 540 °C (T18d) obtained in the C_2H_4 measurement plan. Reaction conditions: 530°C, 1 bar, 32 mm catalyst bed, 40 ml/min, 30 wt% MoO_3/γ-Al_2O_3.

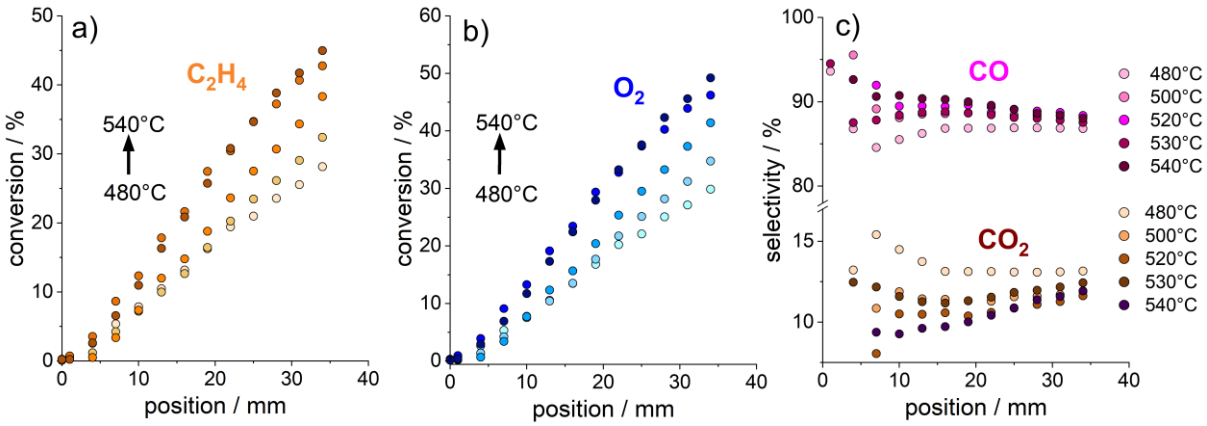

Figure S 12: C_2H_4 (a), O_2 (b) conversion profiles and CO (c) selectivity profiles measured at 480 (T18a), 500 (18b), 520 (T18c), 530 (T18) and 540 °C (T18d) obtained in the C_2H_4 measurement plan. Reaction conditions: 530°C, 1 bar, 32 mm catalyst bed, 40 ml/min, 30 wt% MoO_3/γ-Al_2O_3.

3.2.4 Mars-Van Krevelen Model

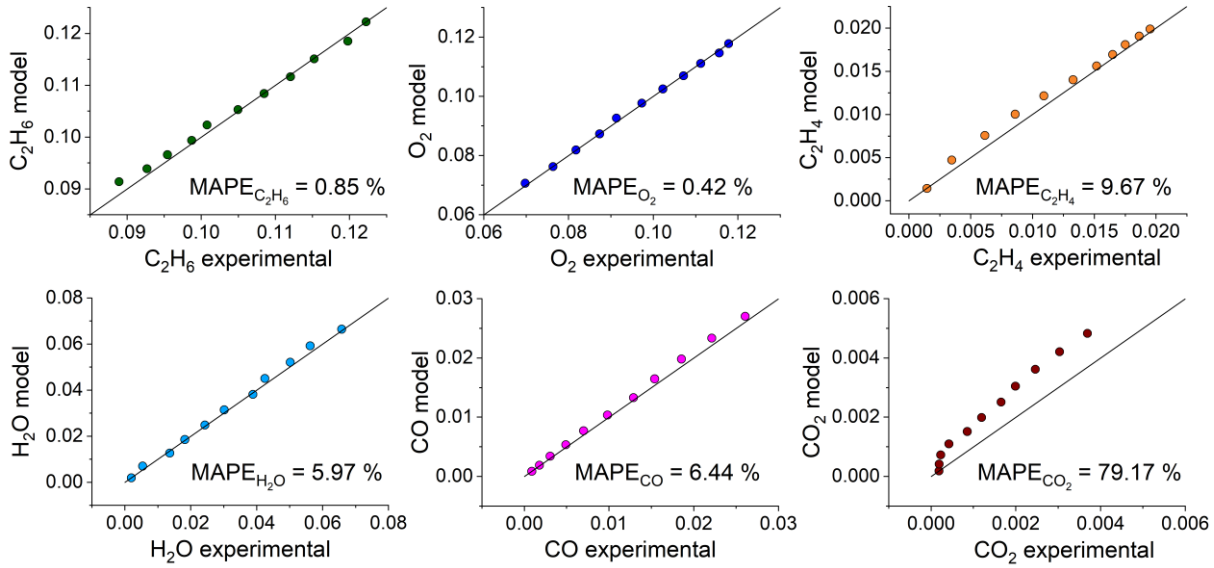

Figure S 13: Predicted components versus corresponding experimental results (P13) are shown (parity plots). Reaction conditions: C_2H_6/O_2:10/10, 530°C, 1 bar, 32 mm catalyst bed, 30 ml/min, 30 wt% MoO_3/γ-Al_2O_3.

3.3.2 Spatial Spectroscopic Profile

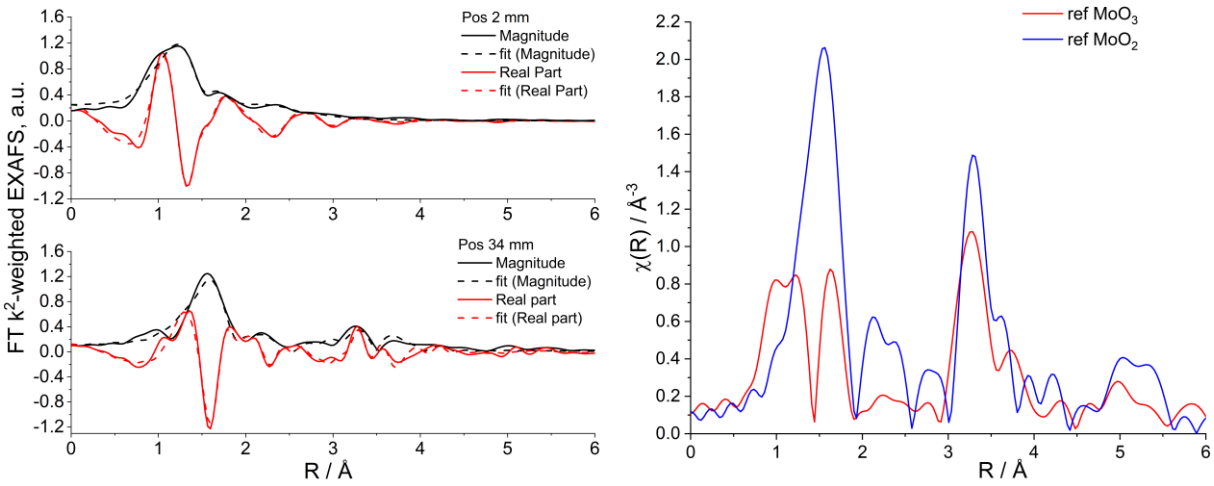

Figure S 14: FT k2-weighted EXAFS spectra measured operando during the oxidative dehydrogenation of ethane to ethylene over MoO_3/γ-Al_2O_3 at Mo K edge (530 °C, C_2H_6:O_2 = 10:10) a) at the beginning (position 2 mm) and b) at the end (position 34 mm) of the catalyst bed. c) Reference spectra of bulk MoO_3 and MoO_2.

Supplementary

References

[1] D. Thoenes, H. Kramers, Mass transfer from spheres in various regular packings to a flowing fluid, Chem. Eng. Sci. 8 (1958) 271–283. https://doi.org/10.1016/0009-2509(58)85034-4.

[2] R.B. Bird, W.E. Stewart, E.N. Lightfoot, Transport phenomena, Rev. second. ed., Wiley, New York, 2007.

[3] D.E. Mears, Tests for Transport Limitations in Experimental Catalytic Reactors, Ind. Eng. Chem. Proc. Des. Dev. 10 (1971) 541–547. https://doi.org/10.1021/i260040a020.

[4] G. Ertl, H. Knözinger, F. Schüth, J. Weitkamp (Eds.), Handbook of heterogeneous catalysis, 2nd ed., Wiley-VCH, Weinheim, 2008.

[5] D.E. Mears, Diagnostic criteria for heat transport limitations in fixed bed reactors, J. Catal. 20 (1971) 127–131. https://doi.org/10.1016/0021-9517(71)90073-X.